Osteocyte *Sptbn1* deficiency alters cell survival and mechanotransduction following formation of plasma membrane disruptions (PMD) from mechanical loading

Mackenzie L. Hagan[1], Anik Tuladhar[1], Kanglun Yu[1], Dima W. Alhamad[1], Husam Bensreti[1], Jennifer Dorn[1], Victor M. Piedra[1], Nicholas Cantu[1], Eric G. Stokes[1], Daniel Blumenthal[1], Rachel L. Roberts[1], Vanshika Balayan[1], Sarah M. Bass[1], Thomas Dickerson[1], Anabel Liyen Cartelle[1], Marlian Montesinos-Cartagena[1], Mohamed E. Awad[2], Alberto A. Castro[3], Theodore Garland, Jr.[3], Marion A. Cooley[2], Maribeth Johnson[4], Mark W. Hamrick[1], Paul L. McNeil[1], Meghan E. McGee-Lawrence[1,5+]

[1]Department of Cellular Biology and Anatomy, Medical College of Georgia, Augusta University, 1460 Laney Walker Blvd, CB1101, Augusta, GA, USA

[2]Department of Oral Biology and Diagnostic Sciences, Dental College of Georgia, Augusta University, Augusta, GA

[3]Evolution Ecology & Organismal Biology Department, University of California Riverside

[4]Department of Neuroscience and Regenerative Medicine, Medical College of Georgia, Augusta University, Augusta GA

[5]Department of Orthopaedic Surgery, Augusta University, Augusta, GA

Running Head: Osteocyte *Sptbn1* deficiency and PMD formation

+Corresponding Author:
Meghan E. McGee-Lawrence, Ph.D.
Department of Cellular Biology and Anatomy,
Medical College of Georgia. Augusta University
1460 Laney Walker Blvd., CB1101 Augusta GA 30912
Phone: (706) 446-0128
Fax: (706) 721-6120
Email: mmcgeelawrence@augusta.edu

KEYWORDS:
Osteocyte, β2-spectrin, mechanotransduction, plasma membrane, mechanical loading

Abstract

We and others have shown that application of high-level mechanical loading promotes the formation of transient plasma membrane disruptions (PMD) which initiate mechanotransduction. We hypothesized that increasing osteocyte cell membrane fragility, by disrupting the cytoskeleton-associated protein β2-spectrin (Sptbn1), could alter osteocytic responses and bone adaptation to loading in a PMD-related fashion. In MLO-Y4 cells, treatment with the spectrin-disrupting agent diamide or knockdown of Sptbn1 via siRNA increased the number of PMD formed by fluid shear stress. Primary osteocytes from an osteocyte-targeted DMP1-Cre Sptbn1 conditional knockout (CKO) model mimicked trends seen with diamide and siRNA treatment and suggested the creation of larger PMD, which repaired more slowly, for a given level of stimulus. Post-wounding cell survival was impaired in all three models, and calcium signaling responses from the wounded osteocyte were mildly altered in Sptbn1 CKO cultures. Although Sptbn1 CKO mice did not demonstrate an altered skeletal phenotype as compared to WT littermates under baseline conditions, they showed a blunted increase in cortical thickness when subjected to an osteogenic tibial loading protocol as well as evidence of increased osteocyte death (increased lacunar vacancy) in the loaded limb after 2 weeks of loading. The impaired post-wounding cell viability and impaired bone adaptation seen with Sptbn1 disruption support the existence of an important role for Sptbn1, and PMD formation, in osteocyte mechanotransduction and bone adaptation to mechanical loading.

Introduction

Osteocytes embedded within the bone extracellular matrix sense mechanical loads placed on the skeleton and direct downstream adaptation via signaling to osteoblasts and osteoclasts, where higher-level impact loads induce a greater osteogenic response as compared to more gradual application of loading [1-5]. Although fluid flow shear stress has been identified as a key component of osteocyte mechanosensation, the precise molecular mechanisms that osteocytes use to detect mechanical stimuli are still being elucidated. *In vitro* studies have shown strong support for the relevance of gap junctions and Connexin43 hemichannels [6-12], integrins [13, 14], TRPV4 channels and microtubules [15] and Piezo channels [16] in processes of osteocyte mechanosensation. However, none of these mechanisms have yet fully explained how osteocytes sense and respond to higher levels (e.g., impact loads) of mechanical stimuli *in vivo*. We believe osteocytes utilize the proposed methods above, but in addition, develop small, repairable plasma membrane disruptions (PMD) both *in vitro* and *in vivo* in response to higher levels of mechanical loading [17-21], and that these PMD may serve as an additional mechanosensation mechanism for osteocytes at these high levels of load (e.g., >30 dynes/cm^2). Osteocyte PMD formation likely occurs via drag forces applied to the osteocyte pericellular matrix around dendrites during loading-induced fluid shear [20]. However, the relative importance of PMD in osteocyte mechanosensation and subsequent bone adaptation has not been rigorously tested.

Mechanosensitive tissues, such as epithelial cells and myocytes, also develop PMD with mechanical loading and show evidence of mechanotransduction downstream of these PMD [22-31]. Importantly, previous studies in such tissues revealed that one effective strategy to test PMD relevance in mechanosensation is to alter PMD susceptibility and observe downstream effects on

74 associated tissue adaptation. For example, in myocytes, absence of the cytoskeletal structural
75 protein dystrophin promoted increased PMD formation both under normal loading conditions (e.g.,
76 normal cage activity) and with exposure to exercise [32]. The absence of dystrophin in mice (e.g.,
77 the *mdx* mouse model) increased the fragility of the myocyte plasma membranes, resulting in the
78 formation of more frequent, larger plasma membrane disruptions that were more difficult to repair
79 and survive [32]. Ultimately, this promoted atrophy of the tissue as the progenitor cell pool used
80 to replenish lost myocytes became depleted. These observations led us to the question whether
81 modulating plasma membrane integrity in osteocytes would affect PMD development and
82 subsequent downstream bone adaptation to mechanical loading.

83

84 Although osteocytes do not express dystrophin, they do abundantly express the structurally similar
85 protein non-erythrocytic 1 spectrin β (also known as βII spectrin, a product of the *Sptbn1* gene).
86 This protein is particularly prevalent in the dendritic processes that are important for detection of
87 mechanical loading [7, 33, 34]. Members of the spectrin super-family of proteins, such as *Sptbn1*
88 and dystrophin, bind F-actin to ankyrin to provide structural support to the plasma membrane.
89 *Sptbn1* has already been implicated as an important mediator of skeletal health, as polymorphisms
90 in the *SPTBN1* locus were linked to low bone mineral density (BMD) and fracture risk in several
91 human genome-wide association studies (GWAS) [35-37]. The molecular mechanisms behind this
92 association are not currently known. We hypothesized that disrupting the osteocyte spectrin
93 network would lead to increased osteocyte membrane fragility, resulting in greater susceptibility
94 to PMD formation, allowing a mechanistic investigation into the effect of PMD in osteocytic
95 responses to mechanical loading and subsequent bone adaptation. We used genetic and
96 pharmacological approaches to disrupt Sptbn1 both in vitro and in vivo, testing the effect of these

manipulations on osteocyte PMD formation, repair rate, post-wounding survival, and responses to loading.

Materials and Methods

Sptbn1 CKO mouse model

All animal experiments followed NIH guidelines and were approved by the Institutional Animal Care and Use Committee at Augusta University. Osteocyte-targeted male and female *Sptbn1* conditional knockout (CKO) mice were generated by crossed *Sptbn1* floxed mice (JAX #020288, exon 3 floxed) with the 10 kb DMP1-Cre mouse (JAX #023047) to generate *Sptbn1*$^{fl/fl}$: Dmp1 Cre+ mice (hereafter referred to as *Sptbn1* CKO). Cre-negative *Sptbn1* floxed littermates (*Sptbn1* $^{fl/fl}$: Dmp1-Cre-) served as wildtype littermate controls (hereafter referred to as WT). All mice were housed in standard rodent cages with a 12-hr light/ 12-hr dark schedule and were permitted water and standard rodent chow *ad libitum*.

In vitro studies

Osteocyte cell culture

MLO-Y4 cells were maintained in growth medium (α-MEM +5% fetal bovine serum (FBS, Atlanta Biologicals) +5% bovine calf serum (HyClone) +1% Penicillin/Streptomycin). Primary osteocytes were isolated from long bone diaphyses (femur, tibia, and humerus) of Sptbn1 CKO mice and WT littermates as described [20]. Cells were plated onto type 1 collagen-coated dishes and grown to 70% confluency, at which time cells were re-seeded for all subsequent experiments.

All primary osteocyte experiments were conducted within 2 weeks of isolation, as recommended [38].

RNAscope analysis of Sptbn1 expression

Deficiency in *Sptbn1* expression for the Sptbn1 CKO model was confirmed in primary osteocytes via RNAscope. Primary osteocytes were grown for 10 days in type 1 collagen coated 10 cm dishes. On the 11th day, the cells were seeded onto glass slides coated with type 1 collagen at a density of 40,000 cells/slide. Cells were grown for 4 days more days on the glass slides, then fixed with 4% formaldehyde, dehydrated, and stored in the –20°C freezer. On the day of the experiment, the slides were rehydrated and processed according to the protocol provided by Advanced Cell Diagnostics (ACD). Briefly, the slides were exposed to hydrogen peroxide for 10 min, then protease III for 10 min. Sptbn1 probe (#546241) was added to the slides for 2 hours in the HybEZ™ II oven. Slides were left overnight in 5x saline sodium citrate buffer. The next day, the signal was amplified using the RNAscope® Multiplex Fluorescent Reagent Kit v2 (# 323100). HRP-C1 was added for 15 min, followed by TSA Vivid™ Fluorophore 520 for 30 min, then by HRP blocker for 15 min. The nucleus was stained with Hoechst and slides were mounted using Vectamount aqueous mounting media (#101098-068). Slides were imaged with a 40x objective using a Leica STELLARIS confocal microscope.

Sptbn1 disruption via diamide treatment and siRNA

To test the effects of Sptbn1-disruption in immortalized osteocytes, MLO-Y4 cells were treated with diamide (500μM; 10 minutes prior to wounding) as previously described [34]. Effects of

diamide treatment on the integrity of the spectrin network were assessed via immunocytochemical staining using a commercial antibody (anti-Sptbn1, abcam #ab72239). F-actin was visualized using TRITC-labeled phalloidin (Sigma #P1951) and nuclei were stained with DAPI. Maximum fluorescence intensity for each channel was calculated for individual cells. For siRNA studies, MLO-Y4 cells were transfected with an siRNA against *Sptbn1* (Santa Cruz #270043) or a scrambled control (Santa Cruz #37007) using a commercial transfection reagent (Lipofectamine RNAiMax; ThermoFisher Scientific #13778075). Studies were initiated 72 hours after transfection.

RNA isolation and PCR analysis

RNA was isolated from cell lysates as previously described [39]. Reverse transcription was performed using a commercially available reverse transcription kit (Invitrogen Superscript III), where the final concentration of cDNA was 2000 ng/ µL. Semi-quantitative PCR (qPCR) was performed using SYBR green PCR kit (Qiagen Quantitect #204143) on a BioRad CFX Connect PCR system. Each PCR reaction contained 37.5 ng cDNA. Primer sequences were as follows: Gapdh_F: 5'-GGGAAGCCCATCACCATC-3', Gapdh_R: 5'-GCCTCACCCCATTTGATGTT-3', Sptbn1_F: 5'-CAGCACCTTGGCCTCACTAA-3'; Sptbn_R: 5'-CCAATGCGCTTTCCTTCGAC-3'.

Laser wounding – analysis of PMD repair rates

Osteocytes were seeded into 60-mm dishes in osteocyte culture medium and wounded with an 820nm multiphoton laser in PBS containing calcium (1.8 mM) and FM1-43 dye (3 µM), as we

previously described [21]. One PMD per osteocyte, located on a dendritic process, was created. To estimate PMD size, FM1-43 dye influx was measured as area under the curve (AUC) over the first 40 seconds of the experiment (i.e., during the phase of exponential, rapid dye influx prior to plateau from repair) [20, 21]. To quantify PMD repair rate, the derivative of the FM1-43 fluorescence versus time curve was calculated to permit analysis of the curve slope, indicative of repair rate quantified as the AUC of this slope vs. time curve [20].

Laser wounding – calcium signaling

Osteocytes were loaded with Cal-520-AM dye (catalog # 171868), after which calcium signaling was initiated by a laser-induced PMD as described [20]. Transmission of calcium signaling to non-wounded adjacent cells was quantified as previously described [20], measured as the number of non-wounded cells with Cal-520AM fluorescence exceeding background levels after laser firing and the AUC of the fluorescence vs. time curves for these non-wounded cells.

Fluid flow shear stress

Osteocytes were seeded into type 1 collagen-coated flow chamber slides (Ibidi, µSlide VI$^{0.4}$, #80606; 1,000 cells per channel) and cultured for up to 4 days with fresh media added daily. Cells were subjected to fluid flow shear stress (30 dynes/cm^2) for 5 minutes using a syringe pump (Harvard Apparatus PHD Ultra I/W) and culture medium supplemented with 1 mg/ml of 10 kDa fluorescein-conjugated dextran used as a membrane disruption tracer, as previously described [21]. At the conclusion of experiments, cells were washed 3 times with PBS and imaged on a confocal microscope (Zeiss). Cytosolic retention of fluorescein dextran was interpreted as evidence of a

membrane disruption event; wounded cells permit entry of the dextran molecule, and successful PMD repair seals the tracer inside the cell [21]. The percentage of wounded osteocytes normalized to total cell number was quantified in each experiment. Using parameters described above, varying sizes of fluorescently conjugated dextran (3 kDa, 10 kDa, 70 kDa) were added to the flow medium in replicate experiments to characterize approximate relative PMD size in primary osteocytes isolated from Sptbn1 CKO and WT littermate mice. Three fluid flow shear stress intensities (10, 30, and 50 dynes/cm^2) were independently tested for each size of dextran.

Post-wounding cell survival

For assessment of post-wounding repair and survival, MLO-Y4 osteocytes were wounded by glass beads, as previously described [21] and primary osteocytes isolated from female Sptbn1 CKO and WT mice were subjected to fluid shear as described above (30 dynes/cm^2, 5 minutes). In both flow and bead wounding conditions, cells were stained at least five minutes after wounding with propidium iodide (0.3 μg/mL) to detect dead cells (i.e., unrepaired PMD) and imaged on a confocal microscope (Zeiss) [21]. The percentages of dead cells (PI+) normalized to total cell number were quantified with image analysis software (Bioquant).

In vivo studies

Establishment of voluntary wheel running and uniaxial tibial loading models in wildtype mice

Building upon our previous work using treadmill models, before testing the role of Sptbn1 in osteocyte responses to loading, we wanted to establish which forms of mechanical loading

205 promoted osteocyte PMD formation in mice. We first tested voluntary wheel running, which (like
206 downhill treadmill exercise) has been reported to increase PMD formation in *mdx* mice [40]. As
207 proof of principle, these studies were conducted on mice selectively bred for high voluntary wheel-
208 running activity as well as non-selected control lines. At generation 80, we sampled male and
209 female mice from each of four different "High Runner" mouse lines that had been selectively bred
210 to have high voluntary wheel-running activity and from four non-selected control mouse lines
211 ("Control") as previously described [41, 42]. At 12 weeks of age, beginning six days prior to
212 sacrifice, half of the animals within each group were provided access to a running wheel (Wahman-
213 type activity wheels, 1.12 m circumference, 35.7 cm diameter, 10 cm wide running surface) that
214 permitted voluntary running for 6 days while the remaining mice had no wheel access. All animals
215 received dual subcutaneous injections of calcein 5 days and 1 day prior to sacrifice to label
216 mineralizing bone surfaces.

217

218 As a second model, given recent concerns about off-target expression of Dmp1-Cre in skeletal
219 muscle [43], we established a uniaxial tibial loading protocol which would not require skeletal
220 muscle contraction to induce bone loading. Female CD-1 wildtype mice were subjected to either
221 one bout (acute) or 2 weeks (chronic) of uniaxial tibial loading as previously described [44-46]
222 beginning at 12 weeks of age. Chronic loading of the left tibia was performed three days per week
223 on alternating days; the right tibia for each mouse served as a non-loaded internal control. Mice
224 were anesthetized with isoflurane, and each loading session consisted of 50 loading cycles with a
225 linear ramp to a peak of -11N (~1500με, based on preliminary strain gauging studies; *data not*
226 *shown*), 0.2 sec dwell followed by a linear release at the same rate and another dwell near zero
227 load for 10 sec before the next cycle. All animals received sequential subcutaneous injections of

228 calcein on days 5 and 1 prior to sacrifice to label mineralizing bone surfaces. Mice were sacrificed
229 via carbon dioxide and were immediately perfused with 10% formalin prior to tissue harvest.

230

231 *Tibial loading studies in the Sptbn1 CKO mouse line*

232 *Sptbn1* CKO mice and littermate controls were subjected to either one bout (acute) or 2 weeks
233 (chronic) of uniaxial tibial loading as described above and were administered subcutaneous
234 injections of alizarin complexone 5 days and 1 day prior to sacrifice to label mineralizing bone
235 surfaces for dynamic histomorphometry studies.

236

237 *Osteocyte PMD formation from acute loading*

238 Plasma membrane disruptions were detected in the tibias of mice subjected to wheel running or
239 tibial loading as previously described [19-21]. Bones were decalcified in 15% EDTA, paraffin
240 embedded, sectioned longitudinally, and subjected to immunohistochemistry with a FITC-
241 conjugated mouse albumin antibody (AIFAG3140, Accurate Chemical Corp.) to detect
242 cytoplasmic localization of endogenous albumin as a PMD tracer [19-21]. Sections were
243 counterstained with DAPI (Vectashield) to visualize cell nuclei. Osteocytes presenting with a
244 signal for both DAPI and cytosolic albumin labeling were interpreted as having experienced a
245 PMD. Five images per bone were captured (Zeiss LSM780) and analyzed with Bioquant Osteo
246 (Nashville, TN) to quantify the relative percentage of PMD-labeled osteocytes for each bone.

247

248 *DXA and micro-computed tomography (microCT) analysis of cortical bone geometry*

Sptbn1 CKO mice and littermate WT controls were subjected to dual-energy x-ray absorptiometry (DXA; Kubtec Digimus software) analysis for quantification of whole body bone mineral density (BMD) at 1 month and 5 months of age under isoflurane anesthesia as previously described [47, 48] to determine whether conditional depletion of Sptbn1 in osteocytes induced a developmental phenotype. BMD was also assessed in isolated tibias collected from the wheel-running High Runner and Control mice; bones were sandwiched between two thin strips of silicone (Walgreens Silicone Scar Sheets) to attenuate x-rays in the absence of overlying soft tissue.

Cortical bone architecture was analyzed in mid-diaphysis of the tibia (proximal to tibia-fibula junction; CD-1 mice and Sptbn1 CKO and WT mice subjected to tibial loading) or mid-diaphysis of the femur (developmental phenotype of Sptbn1 CKO mice) by *ex vivo* μCT (Skyscan 1272), as previously described [19, 49]. Scanning parameters were as follows: source voltage = 70 kV, source current = 142 μA, exposure 897 ms/frame, average of 3 frames per projection, rotation step = 0.600 degrees and 0.25 mm aluminum filter. The specimens were scanned at high resolution (1224 × 820 pixels) with an isotropic voxel size of 9.49 μm. Reconstructions for X-ray projections were performed using the Bruker micro-CT Skyscan software (NRecon, and DataViewer) (v. 1.7.3.1, Brüker micro-CT, Kontich, Belgium). Ring artifact and beam hardening corrections were applied in reconstruction. Datasets were loaded into CTAnalyser software vs. 1.20.3.0 (Skyscan) and region and volume of interest were selected from the reconstructed image stacks. Properties (9-13 μm/voxel resolution) were calculated with the manufacturer's software. For the wheel-running High Runner and Control mice, the mid-diaphysis of each femur was analyzed for a subset of mice by micro-computed tomography (Skyscan 1174, 19 μm resolution), and cortical bone properties were quantified with the manufacturer's software (CTAn) as described above.

272

273 *Dynamic histomorphometry analysis of cortical bone formation*

274 Bones were embedded in methyl methacrylate for dynamic histomorphometry as previously
275 described [50]. Briefly, cross-sections were cut from the mid-diaphysis with a low-speed diamond
276 saw (Buehler Isomet) and hand polished on a grinding wheel (Buehler Ecomet) as needed to <100
277 μm thickness. Sections were mounted on glass slides (Cytoseal™ XYL) and imaged with an
278 epifluorescent microscope (Olympus IX-70) and digital camera (QIcam). Periosteal and
279 endocortical mineral apposition rates (MAR, μm/day) and mineralizing surfaces (MS/BS, %) were
280 quantified with image analysis software (Bioquant OSTEO, Nashville TN) as previously described
281 [50, 51].

282

283 *Lacunar occupancy*

284 Thin (10 μm) longitudinal tibial sections were obtained from the methyl methacrylate blocks of
285 the mice subjected to 2 weeks of tibial loading and from the paraffin blocks of mice subjected to
286 one bout of acute loading. Sections were stained with Goldner's Trichrome to determine osteocyte
287 lacunar vacancy as a measure of cell viability as previously described [50]. Bone sections were
288 examined at 400× magnification, and a total of 10 images per bone were collected at random
289 locations throughout the cortical bone. The percentage of empty osteocyte lacunae was quantified
290 with image analysis software (Bioquant Osteo).

291

292 *Statistics*

For all datasets, sample sizes for each experiment are described in the respective figure legends and tables. Datasets with two conditions were analyzed by pooled t-tests or matched pair t-tests (the latter used when comparing loading responses between loaded vs. non-loaded limbs within the same mouse). For tibial loading studies in the Spbn1 CKO mouse line, the percent difference in each bone property measured by microCT and dynamic histomorphometry between the loaded left tibia and the non-loaded right tibia was calculated for each mouse as: *% difference* = [*bone property* $_{\text{left tibia}}$ − *bone property* $_{\text{right tibia}}$] / *bone property* $_{\text{right tibia}}$ (where *bone property* = cortical bone area, cortical bone thickness, etc.) to assess relative changes in bone properties with loading. Datasets with more than two conditions were analyzed by ANOVA with interaction effects followed by Fisher's LSD post-hoc tests as appropriate. JMP Pro statistical analysis software (v. 17.0.0; SAS Institute) was used for all analyses and alpha=0.05 used to determine statistical significance. Grubb's extreme studentized deviate test (GraphPad) was used to exclude a maximum of one extreme outlier per group as needed [52].

For the wheel-running experiments with High Runner and Control lines of mice, with the exception of microCT datasets (which were not available for mice from every line), data were analyzed as mixed models in SAS procedure MIXED with restricted maximum likelihood estimation and Type III tests of fixed effects (e.g., [41, 42, 53]). Selection for High Runner characteristics (Selection or "Linetype"; HR vs. C), sex, and mini-muscle status (see below) were fixed main effects. Replicate line was a random effect nested within linetype. All of these main effects and their interactions were tested relative to the variance among lines, with 1 and 6 degrees of freedom (df), as dictated by the design of the selection experiment. Mini-muscle status was tested relative to the residual df. As previously described, the mini-muscle phenotype is characterized primarily by a

316 50% reduction in hind limb muscle mass [54, 55]. The underlying genetic variant is a C-to-T
317 transition located in a 709-bp intron between exons 11 and 12 of the Myosin heavy polypeptide 4
318 gene [56] that behaves as a simple Mendelian recessive [54]. Mini-muscle status was determined
319 based on a comparison of triceps surae muscle masses in relation to body mass [54]. As our
320 primary focus was determining effects of wheel access and possible differences between High
321 Runner and Control lines, we do not discuss mini-muscle effects in the text. However, all
322 statistical results can be found in **Supplemental Table 2**.

323

324 **Results**

325 *Validation of osteocyte Sptbn1-disrupting strategies.* Before testing the role of Sptbn1 in osteocyte
326 PMD formation and osteocytic responses to loading, we first examined the efficacy of our intended
327 strategies for disrupting Sptbn1 in osteocytes. While we first attempted western blotting for βII-
328 spectrin protein levels in lysates from primary osteocytes isolated from Sptbn1 CKO and WT
329 littermate mice, βII-spectrin is a large molecular weight protein (~274 kDa), and we encountered
330 difficulty in consistently detecting proteins of this size on western blots (data not shown).
331 However, primary osteocytes isolated from the Sptbn1 CKO mice showed a reduction in Sptbn1
332 mRNA signal as visualized by RNAscope as compared to primary osteocytes from WT littermates
333 (**Figure 1A**). Similarly, RNA isolated from MLO-Y4 cells treated with a Sptbn1 siRNA (72 hours
334 after transfection) showed a significant reduction in Sptbn1 gene expression by qPCR as compared
335 to either un-transfected controls or cells transfected with a scrambled control siRNA ($p<0.0001$;
336 **Figure 1B**). We also employed a pharmacological approach, subjecting MLO-Y4 cells to
337 treatment with diamide (a thiol-oxidizing agent known to disrupt the spectrin network) which

338 significantly reduced the immunohistochemical staining fluorescence intensity for Sptbn1 as
339 previously reported [34] (**Figure 1C-D**).

340

341 *Disruption of the osteocyte spectrin network increased the relative abundance and size of osteocyte*
342 *PMD formation during in vitro loading*. To assess *in vitro* osteocyte PMD formation under
343 mechanical loading conditions, osteocytes were exposed to fluid flow shear stress at 30 dynes/cm^2
344 in the presence of a membrane impermanent fluorescent dextran tracer (FDx; 10 kDa). Cells were
345 grown for at least 2 days prior to experiments to promote the formation of a pericellular matrix
346 [20]. As we previously observed no uptake of PMD tracers in the absence of applied shear stress
347 [21], cells were only imaged at the conclusion of loading. MLO-Y4 osteocytes treated with
348 diamide (**Figure 2A**) or Sptbn1 siRNA (**Figure 2B**) displayed significantly more PMD following
349 5 minutes of exposure to fluid shear. Studies were repeated using primary osteocytes isolated from
350 Sptbn1 CKO and WT littermate mice, where we employed three shear stress rates (10 dynes/cm^2,
351 30 dynes/cm^2, and 50 dynes/cm^2) as well as three different sizes of fluorescent dextran molecules
352 (3 kDa, 10 kDa, and 70 kDa) in an effort to assess the impact of Sptbn1 knockdown on PMD size,
353 represented by the relative size of the tracer able to enter the cell under each flow profile as
354 described in previous studies [17, 18]. Using methodology previously described to estimate the
355 molecular radius of each fluorescent tracer [18, 57], we estimated that the molecular radii of 3, 10,
356 and 70 kDa dextran molecules (reflective of the PMD size necessary to permit these dyes to enter
357 the cell) were 0.95 nm, 1.42 nm, and 2.72 nm, respectively. As seen with diamide and Sptbn1
358 siRNA, primary osteocytes from Sptbn1 CKO mice developed more osteocyte PMD with shear
359 stress ($p_{genotype} = 0.0022$) (**Figure 2C-D**), suggestive of increased susceptibility to PMD formation.
360 Flow rate was also associated with PMD abundance, with more PMD occurring at higher levels of

shear stress as we previously reported ($p_{Flow\ Rate} = 0.0051$) [21], whereas dextran tracer size was inversely related to PMD abundance ($p_{FDX\ Size} < 0.0001$), with few osteocytes showing intracellular presence of the 70 kDa tracer after flow even at the highest levels of shear (**Figure 2C-D**); this latter result suggests that the majority of PMD formed at these shear levels have a radius of less than 2.7 nm in size, as they did not permit entry of the 70 kDa tracer. However, we observed a trend for an interaction between genotype and dextran size ($p_{Genotype\ x\ FDX} = 0.0811$); this result suggests that the Sptbn1 CKO cultures tended to show greater intracellular presence of the larger fluorescent dextran molecules for a given level of shear stress, suggesting the possibility of increased PMD size in Sptbn1 CKO as compared to WT osteocytes (**Figure 2C-D**).

PMD repair rate was slower in Sptbn1-targeted osteocytes. Given the data suggesting increased susceptibility and size of osteocyte PMD in the Sptbn1-disrupted osteocytes, we quantified PMD repair rates using previously established methodology [20, 21, 50]. Consistent with the idea of increased PMD size with Sptbn1 disruption seen in fluid shear stress studies, we observed a trend for increased FM1-43 dye influx immediately after creation of laser-induced PMD (as measured by area under the curve) in Sptbn1 CKO osteocytes ($p_{genotype} = 0.0779$) as compared to WT controls in laser wounding experiments, specifically in the first 40 seconds after wounding (**Figure 3A**). Increased influx of FM1-43 in the earliest time points of the laser wounding experiment suggests rapid influx of membrane-impermeant dye consistent with the formation of a larger PMD. The derivative of the FM1-43 fluorescence versus time curve was calculated to permit analysis of the curve slope, indicative of repair rate, which was quantified as the AUC of this slope vs. time curve as described in our previous studies [20]. The area under the curve of these slope vs. time graphs

383 was significantly increased in the Sptbn1 CKO osteocytes ($p_{genotype}$ = 0.0442), indicative of a
384 slower rate of PMD repair (**Figure 3B**).

385

386 *Post-wounding cell survival was decreased with Sptbn1 disruption*. Slow PMD repair can promote
387 post-wounding cell death [20, 50]. To test whether the increased susceptibility to PMD, larger
388 PMD size, and/or slower repair would impact post-wounding cell survival, we employed a
389 mechanical wounding assay with glass beads. Cells were stained with propidium iodide after
390 wounding to detect non-repaired (i.e., dead) cells. Diamide treatment significantly increased the
391 number of osteocytes that did not survive the wounding event (**Figure 4A**). Notably, diamide in
392 the absence of wounding did not increase cell death in these experiments, further supporting the
393 idea that PMD repair failure, rather than an overall toxic effect of this drug, promoted cell loss
394 (**Figure 4A**). Comparable results were obtained with MLO-Y4 cells treated with Sptbn1-targeting
395 siRNA and primary osteocytes isolated from Sptbn1 CKO mice subjected to fluid shear (**Figure**
396 **4B-C**), where little to no evidence of cell death was seen in the absence of wounding (*data not*
397 *shown*). Together, these results parallel the wounding-induced loss of myocyte viability seen in
398 the *mdx* murine model of muscular dystrophy, which is deficient in the spectrin-family member
399 dystrophin [32, 58-60].

400

401 *Calcium wave propagation from Sptbn1 CKO osteocytes was minimally affected*. Evidence of
402 mildly altered mechanotransduction was observed as a trend for diminished calcium signaling
403 intensity in wounded cells from Sptbn1 CKO as compared to WT cultures ($p_{genotype}$ = 0.0901;
404 **Figure 5A**). We also observed a trend for the Sptbn1 CKO cultures to show an increased

405 proportion of non-wounded neighboring cells initiating calcium signaling following creation of a
406 single PMD in a nearby cell (Figure 6B, $p_{genotype} = 0.0774$) and for increased calcium signaling
407 intensity in the non-wounded neighboring cells ($p_{genotype} = 0.0523$). This observation may be
408 consistent with the increased PMD size and slower rate of PMD repair in the Sptbn1 CKO cultures,
409 as previous studies have shown that PMD repair rate is inversely proportional to the amount of
410 ATP released from a wounded osteocyte [17, 18], but we wish to clearly acknowledge the
411 limitation that none of these experiments reached our threshold to be considered statistically
412 significant ($p<0.05$).

413

414 *Osteocytes from wildtype mice developed PMD from voluntary wheel running and uniaxial tibial*
415 *loading in vivo.* We previously investigated osteocyte PMD formed in wildtype mice during
416 forced downhill treadmill running [20, 21, 50], which is a loading model reported to cause acute
417 myocyte damage in mice that are deficient in the spectrin family member dystrophin (i.e., *mdx*
418 mouse model) [61, 62]. However, we recognized that this loading model has inherent limitations
419 such as its damaging nature and varied effects on bone [63-66], and therefore before investigating
420 the effects of Sptbn1 in osteocyte PMD formation *in vivo*, we first tested whether other forms of
421 mechanical loading could be used to promote osteocyte PMD formation using wildtype mice. We
422 first tested voluntary wheel running, which (like downhill treadmill exercise) has been reported to
423 increase PMD formation in *mdx* mice [40]. These experiments were performed using a previously
424 established "High Runner" wildtype mouse model along with non-selected controls [41, 42], as
425 reliable wheel running performance was previously established in this model. Although a baseline
426 level of osteocyte PMD was detected in the tibia of mice with no wheel access, both the Control
427 and High Runner groups showed a significant increase in the percentage of osteocyte PMD in mice

with access to a wheel as compared to no wheel access (p_{wheel} = 0.0396; **Figure 6A-B**). No differences were observed between Control and High Runner groups in terms of tibial PMD abundance ($p_{selection}$ = 0.4962); however, there was a trend for an interaction effect between wheel access and sex ($p_{wheel\ x\ sex}$ = 0.0779), with female mice tending to show more PMD with wheel access than males (**Figure 6A-B**), consistent with the observation that female HR mice tend to run longer distances and at higher speeds than HR males [41, 67]. No differences were observed between Control and High Runner groups in tibial BMD ($p_{selection}$ = 0.4998) (**Supplemental Figure 1A**), but mice with wheel access had lower tibial BMD values than those without (p_{wheel} = 0.0457) and females had lower tibial BMD values than males (p_{sex} = 0.0195) (**Supplemental Figure 1A**).

For the femur, short-term wheel access did not generally impact cortical bone geometry as measured by microCT (**Supplemental Table 1A**) or cortical bone dynamic histomorphometry (**Supplemental Table 1B**). High Runner mice showed a significant increase in femoral cortical bone area ($p_{selection}$ = 0.0185) but not femoral cortical bone thickness ($p_{Selection}$ = 0.3776) as compared to controls (**Supplemental Table 1A**). Female mice showed higher rates of femoral endocortical mineralizing surface than males (p_{sex} = 0.0312), and somewhat surprisingly, High Runner mice demonstrated reductions in femoral endocortical mineralizing surface as compared to controls ($p_{selection}$ = 0.0100), but few other differences in dynamic indices of cortical bone formation were associated with group, sex, or wheel access in these studies, likely due to the very short duration of wheel access (**Supplemental Table 1B**). A summary of the mixed models SAS analyses for the wheel-running mouse datasets is available as **Supplemental Table 2**.

Since short-term wheel access did not generally impact cortical bone geometry, even in the High Runner mice selected for high voluntary wheel running activity, we decided to explore alternative

models of mechanical loading with which to interrogate the role of Sptbn1 in osteocyte PMD formation and in skeletal responses to loading. We therefore established a uniaxial tibial loading model first using wildtype female CD-1 mice to directly test the impact of bone loading (without muscle involvement) in osteocyte PMD formation. One acute loading bout was associated with a significant ($p=0.0027$) increase in the number of osteocyte PMD in the loaded left limb as compared to the non-loaded right limb (**Figure 6C**). This loading regimen, when repeated on alternating days for two weeks, significantly increased cortical bone thickness (**Supplemental Figure 2A**) but not cortical bone area (**Supplemental Figure 2B**). While periosteal mineral apposition rate was not increased by this protocol (**Supplemental Figure 2C**), loading induced a significant increase in endocortical mineral apposition rate (**Supplemental Figure 2D)** and periosteal and endocortical mineralizing surfaces (**Supplemental Figures 2E-H)**, supporting the osteogenic nature of our loading protocol. No evidence of woven bone formation was observed in any histological sections (**Supplemental Figure 2G-H**), indicating that the loading protocol did not induce tissue-level skeletal damage. We therefore pursued further tibial loading studies with our Sptbn1 CKO mouse line.

Sptbn1 deficiency did not induce a developmental skeletal phenotype but blunted the anabolic response to mechanical loading. Based on cellular phenotype observed from Sptbn1 deficient osteocytes in response to mechanical loading, we anticipated the development of a skeletal phenotype in our Sptbn1 CKO mouse model. Unexpectedly, the Sptbn1 CKO mice did not demonstrate a skeletal phenotype, as measured by DXA, at 1 or 5 months of age (**Supplemental Table 3**). MicroCT analysis of bone architecture confirmed the lack of a developmental (sedentary) cortical bone phenotype at 5 months of age (**Supplemental Table 4**). Mice were then

474 subjected to uniaxial tibial loading, as described above, for 2 weeks beginning at 12 weeks of age
475 as in preliminary studies. Consistent with the lack of a developmental skeletal phenotype, there
476 were no differences in cortical bone architecture between either male or female Sptbn1 CKO and
477 WT littermate mice in the non-loaded right tibia ($p_{genotype} > 0.310$; **Supplemental Figure 3**).
478 However, when subjected to 2 weeks of osteogenic loading, although Sptbn1 CKO mice tended to
479 shown an osteogenic response to loading (**Supplemental Table 5**), Sptbn1 CKO mice showed a
480 significantly lower percent increase in cortical bone thickness between the loaded left tibia as
481 compared to the non-loaded right tibia ($p_{genotype} = 0.0153$; **Figure 7A-C, Supplemental Table 5**),
482 suggesting impaired cortical bone accrual with loading. Analyzing this same dataset in another
483 way, paired t-tests comparing the loaded left vs. non-loaded right tibia for each animal revealed a
484 significant effect of loading ($p_{paired\ t\text{-}test} = 0.0025$), as expected from our preliminary studies with
485 CD-1 mice, but when grouped by genotype, Sptbn1 CKO mice showed a blunted response ($p_{genotype}$
486 $= 0.0101$) (**Figure 7B-C, Supplemental Table 5**). Loading-induced increases in other cortical
487 bone properties, such as cortical bone area were not impacted by genotype (**Supplemental Figure**
488 **4A-B, Supplemental Table 5**). Similarly, dynamic histomorphometric indices of cortical bone
489 formation showed a significant effect of loading, consistent with our preliminary studies with CD-
490 1 mice but were not impacted by genotype (**Supplemental Figure 4C-H**). As in the preliminary
491 studies with CD-1 mice, no evidence of woven bone formation was observed in any histological
492 sections (*data not shown*).

493

494 *Sptbn1 CKO mice showed more empty osteocyte lacunae after 2 weeks of in vivo loading*. As our
495 *in vitro* studies showed increased PMD abundance when Sptbn1 was disrupted (**Figure 2**), we
496 anticipated increased prevalence of PMD formation in Sptbn1 CKO mice subjected to one bout of

497 acute mechanical loading *in vivo*. Interestingly, we did not observe an increased relative abundance
498 of PMD created from one *in vivo* acute loading bout for the Sptbn1 CKO mice (**Figure 8A-B**).
499 This discrepancy could reflect a difference in ability to visualize PMD in tissue sections as
500 compared to cell culture conditions or could also reflect the fact that a repair failure can lead to
501 loss of the intracellular PMD tracer [20, 50], as shown in our *in vitro* studies where dead cells did
502 not retain fluorescent dextran (**Figure 4**). As we observed increased cell death in Sptbn1-disrupted
503 osteocytes subjected to loading in vitro (**Figure 4**), we quantified osteocyte lacunar vacancy,
504 measured as the number of empty lacunae relative to total lacunae number, in our tissue sections.
505 This analysis was performed for the loaded left tibias immediately after a single acute loading
506 bout, but we also quantified osteocyte lacunar vacancy in our mice subjected to 2 weeks of chronic
507 loading, as a previous study suggest that empty lacunae were only visualized 48 hours after
508 osteocyte necrosis had occurred [68]. While no differences in osteocyte lacunar vacancy were
509 observed immediately after a single loading bout (**Figure 8C-D**), Sptbn1 CKO mice subjected to
510 2 weeks of tibial loading demonstrated a significant increase in the number of empty osteocyte
511 lacunae as compared to WT littermates (**Figure 8E-F**).

512

513 **Discussion**

514 Osteocytes likely utilize a range of mechanisms to sense mechanical loads at varying levels of
515 physiological stress, but previous studies suggest that high-level loading conditions can promote
516 the formation of osteocyte PMD which initiate mechanotransduction events [18-21, 69]. Modeling
517 studies support the idea that osteocytic processes may be exposed to shear stresses of more than
518 50 dynes/cm^2 in vivo [70, 71] and both previous studies [21] as well as results presented here
519 suggest that PMD are readily formed at these levels of loading. Importantly, preceding reports

520 demonstrated that the development of loading-induced PMD in osteocytes and other cell types can
521 be experimentally modulated [69]. We initially reported that Vitamin E deprivation promoted
522 osteocyte PMD development in mice following mechanical loading (downhill treadmill running)
523 by increasing the ROS production [19]. We also showed that increased ROS production and
524 changes in pericellular matrix deposition affected PMD development with aging and were
525 potentially implicated in age-related loss of osteocytes [20]. However, these studies were largely
526 observational in nature; the goal of the current study was to experimentally modulate the integrity
527 of the spectrin network in osteocytes to determine if increasing osteocyte cell membrane fragility
528 would affect osteocytic responses to loading. Results presented here suggest that disrupting the
529 spectrin network in osteocytes increased the propensity for PMD formation at a given level of
530 loading and decreased the likelihood of post-wounding osteocyte survival.

531

532 Although the mechanisms used by osteocytes to respond to different intensities of loading are still
533 debated, several points of consistency have emerged in previous literature. Fluid shear produces
534 larger strains at the cellular level and greater downstream mechanotransduction responses (like
535 nitric oxygen release) as compared to mechanical strain on the extracellular matrix [72-74]. The
536 dendritic processes inside canaliculi are exposed to the greatest shear stresses [70, 75], and the
537 processes, rather than cell bodies, are the key site of mechanosensation in the osteocyte [7, 76, 77].
538 Both previous studies [33, 34] and results presented here demonstrate that βII-spectrin is highly
539 expressed in osteocytic processes where PMD preferentially formed with loading [21]. Spectrin
540 expression in osteocytes was previously linked to mechanotransduction events such as nitric oxide
541 secretion and calcium signaling [34], with spectrin disruption via diamide treatment leading to
542 increased nitric oxide release by osteocytes, whereas our calcium signaling studies did not show a

543 significant effect of Sptbn1 CKO genetic deletion on this early mechanotransduction event, despite
544 a slight, non-significant tendency ($p_{genotype}$ = 0.0774) for Sptbn1 deletion to promote calcium
545 signaling transmission to non-wounded cells in close proximity to the wounded osteocyte. Also,
546 while we recently reported that application of osteocyte PMD-inducing turbulent fluid shear stress
547 [20] increases expression of Cox-2 in osteocytes [78], we also acknowledge the considerable
548 limitation that the studies presented here did not specifically investigate the roles of Sptbn1 and
549 osteocyte PMD formation in more mechanistic responses to mechanical loading such as changes
550 in Wnt signaling or osteocytic control of bone remodeling (e.g., Rankl/Opg expression). Future
551 studies more closely focused on mechanotransduction events will be needed to fully define the
552 role of Sptbn1, and PMD formation, in osteocytic responses to mechanical loading.

553

554 The Sptbn1 locus has been identified in several human genome-wide association studies as being
555 linked to bone mineral density [36, 79], as well as risk of fracture and susceptibility to osteoporosis
556 [80-84]. Further studies utilizing bone co-expression networks constructed from murine cortical
557 bone data suggested that the Sptbn1 locus was causal for regulation of bone mineral density [35].
558 A recent report by Xu et al demonstrated that Sptbn1 expression, as measured by immunostaining
559 in the distal femur, was reduced in 9- vs. 3-month old C57BL/6 mice as well as in ovariectomized
560 as compared to sham-operated female mice [85]. The authors further used viral methods to silence
561 and overexpress Sptbn1 in the bone niche *in vivo*, showing that further suppression of Sptbn1
562 expression exacerbated osteopenic phenotypes while overexpression of Sptbn1 promoted rescue
563 [85]. These effects, however, were attributed to beneficial impacts in osteoblasts and endothelial
564 cells, as Sptbn1 expression positively regulated osteoblast proliferation and differentiation as well
565 as expression of vascular endothelial growth factor [85]; effects on osteocytes, including osteocyte

viability, were unfortunately not reported. As Dmp1-Cre is reported to show activity in osteoblasts as well as osteocytes [86, 87], we cannot exclude the possibility that the blunted anabolic response to mechanical loading in our Dmp1-Cre Sptbn1 CKO mice was driven by osteoblastic, rather than osteocytic, populations. However, we note that we failed to see a cortical bone skeletal phenotype develop under baseline conditions (in the absence of applied mechanical loading), and the increased osteocyte lacunar vacancy in the chronically loaded (but not acutely loaded) limbs of Sptbn1 CKO mice is consistent with the increased post-wounding cell death seen in our *in vitro* diamide-, Sptbn1 siRNA- and Sptbn1 CKO primary osteocyte studies. Although Dmp1-Cre is also reported to show appreciable expression in muscle [43], the uniaxial tibial loading model used here (which loads bone without requiring voluntary muscular contraction) was selected for study to negate some of this concern.

The role of osteocyte Sptbn1 expression shown here is consistent with the effect of the spectrin family protein dystrophin in skeletal muscle, where changes in the organization or expression of cytoskeletal structural proteins can affect propensity for PMD development. Many studies have shown that myocytes are more susceptible to the development of PMD in the absence of dystrophin [32, 58, 62, 88]. Wheel-running studies using *mdx* dystrophic mice showed that the mean distance covered in individual running bouts was positively correlated with the abundance of myofibers with centrally located nuclei as well as metrics of recent acute muscle damage in quadriceps muscle [88]. We also initially tested a voluntary wheel-running model , showing that wheel access was associated with osteocyte PMD formation, but ultimately selected a tibial loading model to test the mechanical responses of the Sptbn1 CKO mice given the latter model's robust ability to induce osteocyte PMD formation, induce cortical bone gain, address concerns about off-target

589 expression of Dmp1-Cre in skeletal muscle, and reduce the variability of individual mouse
590 responses to wheel access [88].

591

592 In conclusion, building upon previous studies interrogating PMD formation in dystrophin-
593 deficient *mdx* mouse models, we targeted the Sptbn1 network in osteocytes to alter osteocyte
594 plasma membrane fragility and to test the downstream effects of this manipulation on
595 mechanotransduction and bone adaptation. Disruption of Sptbn1 in osteocytes increased PMD
596 formation from fluid shear stress and decreased post-wounding cell viability due to impaired PMD
597 repair. Our *in vivo* experimental results suggest that while osteocyte-targeted Sptbn1 deficient
598 mice do not develop a baseline skeletal phenotype at younger ages, they do show a loading-induced
599 phenotype of blunted cortical bone gain following repeated bouts of mechanical loading associated
600 with loss of osteocyte viability. Taken together, the *in vitro* and *in vivo* work presented here
601 suggests an important role for both Sptbn1 and PMD in osteocyte mechanosensation and
602 subsequent downstream bone adaptation to high level mechanical loading. Understanding the role
603 of PMD-related mechanisms and how they affect mechanotransduction responses in these cases of
604 rapid bone degeneration may prove key to identifying therapeutic targets to prevent or reverse the
605 unloading-induced bone loss.

606

607 **Acknowledgements**

608 This work was funded by the National Science Foundation (NSF BMMB #1727949 to MM-L;
609 NSF IOS #2038528 to TG), NASA (NASA Space Biology Grant #80NSSC21K0274 to MM-L)
610 and the NIH (S10 OD025177, P01 AG036675 Core B). The authors wish to acknowledge the

611 Augusta University Electron Microscopy and Histology Core for histological specimen
612 preparation and the Augusta University Cell Imaging Core for assistance with imaging-related
613 experiments.

614

615 **Conflict of Interest Disclosure**: All authors have no conflicts of interest.

616

References

1. Gomez-Cabello A, Ara I, Gonzalez-Aguero A, Casajus JA, Vicente-Rodriguez G (2012) Effects of training on bone mass in older adults: a systematic review. Sports Med 42:301-325

2. Kontulainen S, Sievanen H, Kannus P, Pasanen M, Vuori I (2003) Effect of long-term impact-loading on mass, size, and estimated strength of humerus and radius of female racquet-sports players: a peripheral quantitative computed tomography study between young and old starters and controls. Journal of bone and mineral research : the official journal of the American Society for Bone and Mineral Research 18:352-359

3. LaMothe JM, Hamilton NH, Zernicke RF (2005) Strain rate influences periosteal adaptation in mature bone. Medical engineering & physics 27:277-284

4. Lima F, De Falco V, Baima J, Carazzato JG, Pereira RM (2001) Effect of impact load and active load on bone metabolism and body composition of adolescent athletes. Med Sci Sports Exerc 33:1318-1323

5. Tam N, Santos-Concejero J, Tucker R, Lamberts RP, Micklesfield LK (2018) Bone health in elite Kenyan runners. J Sports Sci 36:456-461

6. Batra N, Burra S, Siller-Jackson AJ, Gu S, Xia X, Weber GF, DeSimone D, Bonewald LF, Lafer EM, Sprague E, Schwartz MA, Jiang JX (2012) Mechanical stress-activated integrin alpha5beta1 induces opening of connexin 43 hemichannels. Proceedings of the National Academy of Sciences of the United States of America 109:3359-3364

7. Burra S, Nicolella DP, Francis WL, Freitas CJ, Mueschke NJ, Poole K, Jiang JX (2010) Dendritic processes of osteocytes are mechanotransducers that induce the opening of hemichannels. Proceedings of the National Academy of Sciences of the United States of America 107:13648-13653

8. Cheng B, Zhao S, Luo J, Sprague E, Bonewald LF, Jiang JX (2001) Expression of functional gap junctions and regulation by fluid flow in osteocyte-like MLO-Y4 cells. Journal of bone and mineral research : the official journal of the American Society for Bone and Mineral Research 16:249-259

9. Cherian PP, Cheng B, Gu S, Sprague E, Bonewald LF, Jiang JX (2003) Effects of mechanical strain on the function of Gap junctions in osteocytes are mediated through the prostaglandin EP2 receptor. The Journal of biological chemistry 278:43146-43156

10. Jiang JX, Cherian PP (2003) Hemichannels formed by connexin 43 play an important role in the release of prostaglandin E(2) by osteocytes in response to mechanical strain. Cell Commun Adhes 10:259-264

11. Genetos DC, Kephart CJ, Zhang Y, Yellowley CE, Donahue HJ (2007) Oscillating fluid flow activation of gap junction hemichannels induces ATP release from MLO-Y4 osteocytes. Journal of cellular physiology 212:207-214

12. Plotkin LI, Speacht TL, Donahue HJ (2015) Cx43 and mechanotransduction in bone. Current osteoporosis reports 13:67-72

13. Cabahug-Zuckerman P, Stout RF, Jr., Majeska RJ, Thi MM, Spray DC, Weinbaum S, Schaffler MB (2018) Potential role for a specialized beta3 integrin-based structure on osteocyte processes in bone mechanosensation. J Orthop Res 36:642-652

14. McNamara LM, Majeska RJ, Weinbaum S, Friedrich V, Schaffler MB (2009) Attachment of osteocyte cell processes to the bone matrix. Anatomical record 292:355-363

15. James S Lyons HCJ, Robert A Law, Katrina M Williams, Jaclyn P Kerr, Guoli Shi , Ramzi J Khairallah, Stuart S Martin, Konstantinos Konstantopoulos, Christopher W Ward, Joseph P Stains `` (2017) Microtubules Tune Mechanotransduction Through NOX2 and TRPV4 to Decrease Sclerostin Abundance in Osteocytes. Science Signaling

16. Sasaki F, Hayashi M, Mouri Y, Nakamura S, Adachi T, Nakashima T (2020) Mechanotransduction via the Piezo1-Akt pathway underlies Sost suppression in osteocytes. Biochemical and biophysical research communications 521:806-813

17. Mikolajewicz N, Sehayek S, Wiseman PW, Komarova SV (2019) Transmission of Mechanical Information by Purinergic Signaling. Biophys J 116:2009-2022

18. Mikolajewicz N, Zimmermann EA, Willie BM, Komarova SV (2018) Mechanically-stimulated ATP release from murine bone cells is regulated by a balance of injury and repair. Elife 7:e37812

19. Hagan ML, Bahraini A, Pierce JL, Bass SM, Yu K, Elsayed R, Elsalanty M, Johnson MH, McNeil A, McNeil PL, McGee-Lawrence ME (2018) Inhibition of Osteocyte Membrane Repair Activity via Dietary Vitamin E Deprivation Impairs Osteocyte Survival. Calcified tissue international

20. Hagan ML, Yu K, Zhu J, Vinson BN, Roberts RL, Montesinos Cartagena M, Johnson MH, Wang L, Isales CM, Hamrick MW, McNeil PL, McGee-Lawrence ME (2020) Decreased pericellular matrix production and selection for enhanced cell membrane repair may impair osteocyte responses to mechanical loading in the aging skeleton. Aging Cell 19:e13056

21. Yu K, Sellman DP, Bahraini A, Hagan ML, Elsherbini A, Vanpelt KT, Marshall PL, Hamrick MW, McNeil A, McNeil PL, McGee-Lawrence ME (2018) Mechanical loading disrupts osteocyte plasma membranes which initiates mechanosensation events in bone. J Orthop Res 36:653-662

22. Clarke MS, Caldwell RW, Chiao H, Miyake K, McNeil PL (1995) Contraction-induced cell wounding and release of fibroblast growth factor in heart. Circ Res 76:927-934

23. Cooper ST, McNeil PL (2015) Membrane Repair: Mechanisms and Pathophysiology. Physiol Rev 95:1205-1240

689 24. Grembowicz KP, Sprague D, McNeil PL (1999) Temporary disruption of the plasma
690 membrane is required for c-fos expression in response to mechanical stress. Molecular
691 biology of the cell 10:1247-1257

692 25. Hamrick MW, McNeil PL, Patterson SL (2010) Role of muscle-derived growth factors in
693 bone formation. Journal of musculoskeletal & neuronal interactions 10:64-70

694 26. Howard AC, McNeil AK, McNeil PL (2011) Promotion of plasma membrane repair by
695 vitamin E. Nat Commun 2:597

696 27. Howard AC, McNeil AK, Xiong F, Xiong WC, McNeil PL (2011) A novel cellular defect
697 in diabetes: membrane repair failure. Diabetes 60:3034-3043

698 28. Labazi M, McNeil AK, Kurtz T, Lee TC, Pegg RB, Angeli JP, Conrad M, McNeil PL
699 (2015) The antioxidant requirement for plasma membrane repair in skeletal muscle. Free
700 Radic Biol Med 84:246-253

701 29. McNeil PL, Ito S (1989) Gastrointestinal cell plasma membrane wounding and resealing
702 in vivo. Gastroenterology 96:1238-1248

703 30. McNeil PL, Khakee R (1992) Disruptions of muscle fiber plasma membranes. Role in
704 exercise-induced damage. The American journal of pathology 140:1097-1109

705 31. Yu QC, McNeil PL (1992) Transient disruptions of aortic endothelial cell plasma
706 membranes. The American journal of pathology 141:1349-1360

707 32. Bansal D, Miyake K, Vogel SS, Groh S, Chen CC, Williamson R, McNeil PL, Campbell
708 KP (2003) Defective membrane repair in dysferlin-deficient muscular dystrophy. Nature
709 423:168-172

710 33. Kamioka H, Sugawara Y, Honjo T, Yamashiro T, Takano-Yamamoto T (2004) Terminal
711 differentiation of osteoblasts to osteocytes is accompanied by dramatic changes in the
712 distribution of actin-binding proteins. Journal of bone and mineral research : the official
713 journal of the American Society for Bone and Mineral Research 19:471-478

714 34. Wu XT, Sun LW, Yang X, Ding D, Han D, Fan YB (2017) The potential role of spectrin
715 network in the mechanotransduction of MLO-Y4 osteocytes. Sci Rep 7:40940

716 35. Calabrese GM, Mesner LD, Stains JP, Tommasini SM, Horowitz MC, Rosen CJ, Farber
717 CR (2017) Integrating GWAS and Co-expression Network Data Identifies Bone Mineral
718 Density Genes SPTBN1 and MARK3 and an Osteoblast Functional Module. Cell Syst
719 4:46-59 e44

720 36. Chen YC, Guo YF, He H, Lin X, Wang XF, Zhou R, Li WT, Pan DY, Shen J, Deng HW
721 (2016) Integrative Analysis of Genomics and Transcriptome Data to Identify Potential
722 Functional Genes of BMDs in Females. Journal of bone and mineral research : the official
723 journal of the American Society for Bone and Mineral Research 31:1041-1049

37. Hu Y, Tan LJ, Chen XD, Liu Z, Min SS, Zeng Q, Shen H, Deng HW (2017) Identification of Novel Potentially-pleiotropic Variants Associated With Osteoporosis and Obesity Using cFDR method. J Clin Endocrinol Metab

38. Stern AR, Stern MM, Van Dyke ME, Jahn K, Prideaux M, Bonewald LF (2012) Isolation and culture of primary osteocytes from the long bones of skeletally mature and aged mice. Biotechniques 52:361-373

39. McGee-Lawrence ME, Carpio LR, Schulze RJ, Pierce JL, McNiven MA, Farr JN, Khosla S, Oursler MJ, Westendorf JJ (2016) Hdac3 Deficiency Increases Marrow Adiposity and Induces Lipid Storage and Glucocorticoid Metabolism in Osteochondroprogenitor Cells. Journal of bone and mineral research : the official journal of the American Society for Bone and Mineral Research 31:116-128

40. Archer JD, Vargas CC, Anderson JE (2006) Persistent and improved functional gain in mdx dystrophic mice after treatment with L-arginine and deflazacort. FASEB journal : official publication of the Federation of American Societies for Experimental Biology 20:738-740

41. Meek TH, Lonquich BP, Hannon RM, Garland T, Jr. (2009) Endurance capacity of mice selectively bred for high voluntary wheel running. J Exp Biol 212:2908-2917

42. Khan RH, Rhodes JS, Girard IA, Schwartz NE, Garland TG (2024) Does Behavior Evolve First? Correlated Responses to Selection for Voluntary Wheel-Running Behavior in House Mice. Ecological and Evolutionary Physiology 97:97-117

43. Dasgupta K, Lessard S, Hann S, Fowler ME, Robling AG, Warman ML (2021) Sensitive detection of Cre-mediated recombination using droplet digital PCR reveals Tg(BGLAP-Cre) and Tg(DMP1-Cre) are active in multiple non-skeletal tissues. Bone 142:115674

44. Pead MJ, Suswillo R, Skerry TM, Vedi S, Lanyon LE (1988) Increased 3H-uridine levels in osteocytes following a single short period of dynamic bone loading in vivo. Calcif Tissue Int 43:92-96

45. Skerry TM, Bitensky L, Chayen J, Lanyon LE (1988) Loading-related reorientation of bone proteoglycan in vivo. Strain memory in bone tissue? J Orthop Res 6:547-551

46. de Souza RL, Pitsillides AA, Lanyon LE, Skerry TM, Chenu C (2005) Sympathetic nervous system does not mediate the load-induced cortical new bone formation. J Bone Miner Res 20:2159-2168

47. Pierce JL, Sharma AK, Roberts RL, Yu K, Irsik DL, Choudhary V, Dorn JS, Bensreti H, Benson RD, Jr., Kaiser H, Khayrullin A, Davis C, Wehrle CJ, Johnson MH, Bollag WB, Hamrick MW, Shi X, Isales CM, McGee-Lawrence ME (2022) The Glucocorticoid Receptor in Osterix-Expressing Cells Regulates Bone Mass, Bone Marrow Adipose Tissue, and Systemic Metabolism in Female Mice During Aging. Journal of bone and mineral research : the official journal of the American Society for Bone and Mineral Research 37:285-302

762 48. Pierce JL, Ding KH, Xu J, Sharma AK, Yu K, Del Mazo Arbona N, Rodriguez-Santos Z,
763 Bernard P, Bollag WB, Johnson MH, Hamrick MW, Begun DL, Shi XM, Isales CM,
764 McGee-Lawrence ME (2019) The glucocorticoid receptor in osteoprogenitors regulates
765 bone mass and marrow fat. J Endocrinol

766 49. McGee ME MA, Johnson SE, Nelson OL, Robbins CT, Donahue SW (2008) ecreased bone
767 turnover with balanced resorption and formation prevent cortical bone loss during disuse
768 (hibernation) in grizzly bears (Ursus arctos horribilis). Bone

769 50. Hagan ML, Bahraini A, Pierce JL, Bass SM, Yu K, Elsayed R, Elsalanty M, Johnson MH,
770 McNeil A, McNeil PL, McGee-Lawrence ME (2019) Inhibition of Osteocyte Membrane
771 Repair Activity via Dietary Vitamin E Deprivation Impairs Osteocyte Survival. Calcified
772 tissue international 104:224-234

773 51. Dempster DW, Compston JE, Drezner MK, Glorieux FH, Kanis JA, Malluche H, Meunier
774 PJ, Ott SM, Recker RR, Parfitt AM (2013) Standardized nomenclature, symbols, and units
775 for bone histomorphometry: a 2012 update of the report of the ASBMR Histomorphometry
776 Nomenclature Committee. Journal of bone and mineral research : the official journal of the
777 American Society for Bone and Mineral Research 28:2-17

778 52. Grubbs FE (1969) Procedures for detecting outlying observations in samples.
779 Technometrics 11:1-21

780 53. Wallace IJ, Tommasini SM, Judex S, Garland T, Jr., Demes B (2012) Genetic variations
781 and physical activity as determinants of limb bone morphology: an experimental approach
782 using a mouse model. Am J Phys Anthropol 148:24-35

783 54. Garland T, Jr., Morgan MT, Swallow JG, Rhodes JS, Girard I, Belter JG, Carter PA (2002)
784 Evolution of a small-muscle polymorphism in lines of house mice selected for high activity
785 levels. Evolution 56:1267-1275

786 55. Houle-Leroy P, Guderley H, Swallow JG, Garland T, Jr. (2003) Artificial selection for high
787 activity favors mighty mini-muscles in house mice. Am J Physiol Regul Integr Comp
788 Physiol 284:R433-443

789 56. Kelly SA, Bell TA, Selitsky SR, Buus RJ, Hua K, Weinstock GM, Garland T, Jr., Pardo-
790 Manuel de Villena F, Pomp D (2013) A novel intronic single nucleotide polymorphism in
791 the myosin heavy polypeptide 4 gene is responsible for the mini-muscle phenotype
792 characterized by major reduction in hind-limb muscle mass in mice. Genetics 195:1385-
793 1395

794 57. Erickson HP (2009) Size and shape of protein molecules at the nanometer level determined
795 by sedimentation, gel filtration, and electron microscopy. Biol Proced Online 11:32-51

796 58. Claflin DR, Brooks SV (2008) Direct observation of failing fibers in muscles of dystrophic
797 mice provides mechanistic insight into muscular dystrophy. American journal of
798 physiology. Cell physiology 294:C651-658

59. De Luca A, Pierno S, Liantonio A, Cetrone M, Camerino C, Fraysse B, Mirabella M, Servidei S, Ruegg UT, Conte Camerino D (2003) Enhanced dystrophic progression in mdx mice by exercise and beneficial effects of taurine and insulin-like growth factor-1. J Pharmacol Exp Ther 304:453-463

60. Weller B, Karpati G, Carpenter S (1990) Dystrophin-deficient mdx muscle fibers are preferentially vulnerable to necrosis induced by experimental lengthening contractions. J Neurol Sci 100:9-13

61. Quinlan JG, Wong BL, Niemeier RT, McCullough AS, Levin L, Emanuele M (2006) Poloxamer 188 failed to prevent exercise-induced membrane breakdown in mdx skeletal muscle fibers. Neuromuscul Disord 16:855-864

62. Clarke MS, Khakee R, McNeil PL (1993) Loss of cytoplasmic basic fibroblast growth factor from physiologically wounded myofibers of normal and dystrophic muscle. Journal of cell science 106 (Pt 1):121-133

63. Moraska A, Deak T, Spencer RL, Roth D, Fleshner M (2000) Treadmill running produces both positive and negative physiological adaptations in Sprague-Dawley rats. Am J Physiol Regul Integr Comp Physiol 279:R1321-1329

64. Park KS, Lee MG (2015) Effects of unaccustomed downhill running on muscle damage, oxidative stress, and leukocyte apoptosis. J Exerc Nutrition Biochem 19:55-63

65. Rice H, Kurz M, Mai P, Robertz L, Bill K, Derrick TR, Willwacher S (2024) Speed and surface steepness affect internal tibial loading during running. J Sport Health Sci 13:118-124

66. Suito H, Fujikawa K, Ohsako M (2023) Eccentric contractions during downhill running induce Osgood–Schlatter disease in the tibial tuberosity in rats: a focus on histological structures. Sci Rep 13:9863

67. Garland T, Jr., Kelly SA, Malisch JL, Kolb EM, Hannon RM, Keeney BK, Van Cleave SL, Middleton KM (2011) How to run far: multiple solutions and sex-specific responses to selective breeding for high voluntary activity levels. Proc Biol Sci 278:574-581

68. Tatsumi S, Ishii K, Amizuka N, Li M, Kobayashi T, Kohno K, Ito M, Takeshita S, Ikeda K (2007) Targeted ablation of osteocytes induces osteoporosis with defective mechanotransduction. Cell Metab 5:464-475

69. Hagan ML, Balayan V, McGee-Lawrence ME (2021) Plasma membrane disruption (PMD) formation and repair in mechanosensitive tissues. Bone 149:115970

70. Price C, Zhou X, Li W, Wang L (2011) Real-time measurement of solute transport within the lacunar-canalicular system of mechanically loaded bone: direct evidence for load-induced fluid flow. Journal of bone and mineral research : the official journal of the American Society for Bone and Mineral Research 26:277-285

71. Verbruggen SW, Vaughan TJ, McNamara LM (2014) Fluid flow in the osteocyte mechanical environment: a fluid-structure interaction approach. Biomechanics and modeling in mechanobiology 13:85-97

72. Smalt R, Mitchell FT, Howard RL, Chambers TJ (1997) Induction of NO and prostaglandin E2 in osteoblasts by wall-shear stress but not mechanical strain. The American journal of physiology 273:E751-758

73. McGarry JG, Klein-Nulend J, Mullender MG, Prendergast PJ (2005) A comparison of strain and fluid shear stress in stimulating bone cell responses--a computational and experimental study. FASEB journal : official publication of the Federation of American Societies for Experimental Biology 19:482-484

74. Ganesh T, Laughrey LE, Niroobakhsh M, Lara-Castillo N (2020) Multiscale finite element modeling of mechanical strains and fluid flow in osteocyte lacunocanalicular system. Bone 137:115328

75. Anderson EJ, Kaliyamoorthy S, Iwan J, Alexander D, Knothe Tate ML (2005) Nano-microscale models of periosteocytic flow show differences in stresses imparted to cell body and processes. Ann Biomed Eng 33:52-62

76. Thi MM, Suadicani SO, Schaffler MB, Weinbaum S, Spray DC (2013) Mechanosensory responses of osteocytes to physiological forces occur along processes and not cell body and require alphaVbeta3 integrin. Proceedings of the National Academy of Sciences of the United States of America 110:21012-21017

77. Wu D, Schaffler MB, Weinbaum S, Spray DC (2013) Matrix-dependent adhesion mediates network responses to physiological stimulation of the osteocyte cell process. Proceedings of the National Academy of Sciences of the United States of America 110:12096-12101

78. Tuladhar A, Shaver JC, McGee WA, Yu K, Dorn J, Horne JL, Alhamad DW, Hagan ML, Cooley MA, Zhong R, Bollag W, Johnson M, Hamrick MW, McGee-Lawrence ME (2024) Prkd1 regulates the formation and repair of plasma membrane disruptions (PMD) in osteocytes. Bone 186:117147

79. Rivadeneira F, Styrkarsdottir U, Estrada K, Halldorsson BV, Hsu YH, Richards JB, Zillikens MC, Kavvoura FK, Amin N, Aulchenko YS, Cupples LA, Deloukas P, Demissie S, Grundberg E, Hofman A, Kong A, Karasik D, van Meurs JB, Oostra B, Pastinen T, Pols HA, Sigurdsson G, Soranzo N, Thorleifsson G, Thorsteinsdottir U, Williams FM, Wilson SG, Zhou Y, Ralston SH, van Duijn CM, Spector T, Kiel DP, Stefansson K, Ioannidis JP, Uitterlinden AG (2009) Twenty bone-mineral-density loci identified by large-scale meta-analysis of genome-wide association studies. Nat Genet 41:1199-1206

80. Estrada K, Styrkarsdottir U, Evangelou E, Hsu YH, Duncan EL, Ntzani EE, Oei L, Albagha OM, Amin N, Kemp JP, Koller DL, Li G, Liu CT, Minster RL, Moayyeri A, Vandenput L, Willner D, Xiao SM, Yerges-Armstrong LM, Zheng HF, Alonso N, Eriksson J, Kammerer CM, Kaptoge SK, Leo PJ, Thorleifsson G, Wilson SG, Wilson JF, Aalto V, Alen M, Aragaki AK, Aspelund T, Center JR, Dailiana Z, Duggan DJ, Garcia M, Garcia-

Giralt N, Giroux S, Hallmans G, Hocking LJ, Husted LB, Jameson KA, Khusainova R, Kim GS, Kooperberg C, Koromila T, Kruk M, Laaksonen M, Lacroix AZ, Lee SH, Leung PC, Lewis JR, Masi L, Mencej-Bedrac S, Nguyen TV, Nogues X, Patel MS, Prezelj J, Rose LM, Scollen S, Siggeirsdottir K, Smith AV, Svensson O, Trompet S, Trummer O, van Schoor NM, Woo J, Zhu K, Balcells S, Brandi ML, Buckley BM, Cheng S, Christiansen C, Cooper C, Dedoussis G, Ford I, Frost M, Goltzman D, Gonzalez-Macias J, Kahonen M, Karlsson M, Khusnutdinova E, Koh JM, Kollia P, Langdahl BL, Leslie WD, Lips P, Ljunggren O, Lorenc RS, Marc J, Mellstrom D, Obermayer-Pietsch B, Olmos JM, Pettersson-Kymmer U, Reid DM, Riancho JA, Ridker PM, Rousseau F, Slagboom PE, Tang NL, et al. (2012) Genome-wide meta-analysis identifies 56 bone mineral density loci and reveals 14 loci associated with risk of fracture. Nat Genet 44:491-501

81. Liu JM, Zhang MJ, Zhao L, Cui B, Li ZB, Zhao HY, Sun LH, Tao B, Li M, Ning G (2010) Analysis of recently identified osteoporosis susceptibility genes in Han Chinese women. J Clin Endocrinol Metab 95:E112-120

82. Moayyeri A, Hsu YH, Karasik D, Estrada K, Xiao SM, Nielson C, Srikanth P, Giroux S, Wilson SG, Zheng HF, Smith AV, Pye SR, Leo PJ, Teumer A, Hwang JY, Ohlsson C, McGuigan F, Minster RL, Hayward C, Olmos JM, Lyytikainen LP, Lewis JR, Swart KM, Masi L, Oldmeadow C, Holliday EG, Cheng S, van Schoor NM, Harvey NC, Kruk M, del Greco MF, Igl W, Trummer O, Grigoriou E, Luben R, Liu CT, Zhou Y, Oei L, Medina-Gomez C, Zmuda J, Tranah G, Brown SJ, Williams FM, Soranzo N, Jakobsdottir J, Siggeirsdottir K, Holliday KL, Hannemann A, Go MJ, Garcia M, Polasek O, Laaksonen M, Zhu K, Enneman AW, McEvoy M, Peel R, Sham PC, Jaworski M, Johansson A, Hicks AA, Pludowski P, Scott R, Dhonukshe-Rutten RA, van der Velde N, Kahonen M, Viikari JS, Sievanen H, Raitakari OT, Gonzalez-Macias J, Hernandez JL, Mellstrom D, Ljunggren O, Cho YS, Volker U, Nauck M, Homuth G, Volzke H, Haring R, Brown MA, McCloskey E, Nicholson GC, Eastell R, Eisman JA, Jones G, Reid IR, Dennison EM, Wark J, Boonen S, Vanderschueren D, Wu FC, Aspelund T, Richards JB, Bauer D, Hofman A, Khaw KT, Dedoussis G, Obermayer-Pietsch B, Gyllensten U, Pramstaller PP, Lorenc RS, et al. (2014) Genetic determinants of heel bone properties: genome-wide association meta-analysis and replication in the GEFOS/GENOMOS consortium. Human molecular genetics 23:3054-3068

83. Deng YH, Zhao L, Zhang MJ, Pan CM, Zhao SX, Zhao HY, Sun LH, Tao B, Song HD, Wang WQ, Ning G, Liu JM (2013) The influence of the genetic and non-genetic factors on bone mineral density and osteoporotic fractures in Chinese women. Endocrine 43:127-135

84. Wang C, Zhang Z, Zhang H, He JW, Gu JM, Hu WW, Hu YQ, Li M, Liu YJ, Fu WZ, Yue H, Ke YH, Zhang ZL (2012) Susceptibility genes for osteoporotic fracture in postmenopausal Chinese women. Journal of bone and mineral research : the official journal of the American Society for Bone and Mineral Research 27:2582-2591

85. Xu X, Yang J, Ye Y, Chen G, Zhang Y, Wu H, Song Y, Feng M, Feng X, Chen X, Wang X, Lin X, Bai X, Shen J (2021) SPTBN1 Prevents Primary Osteoporosis by Modulating

Osteoblasts Proliferation and Differentiation and Blood Vessels Formation in Bone. Front Cell Dev Biol 9:653724

86. Xiong J, Piemontese M, Onal M, Campbell J, Goellner JJ, Dusevich V, Bonewald L, Manolagas SC, O'Brien CA (2015) Osteocytes, not Osteoblasts or Lining Cells, are the Main Source of the RANKL Required for Osteoclast Formation in Remodeling Bone. PloS one 10:e0138189

87. Lu Y, Xie Y, Zhang S, Dusevich V, Bonewald LF, Feng JQ (2007) DMP1-targeted Cre expression in odontoblasts and osteocytes. J Dent Res 86:320-325

88. Smythe GM, White JD (2011) Voluntary wheel running in dystrophin-deficient (mdx) mice: Relationships between exercise parameters and exacerbation of the dystrophic phenotype. PLoS Curr 3:RRN1295

FIGURE LEGENDS:

Figure 1: Validation of Sptbn1 disrupting strategies for in vitro studies. A) Primary osteocytes isolated from male and female Sptbn1 CKO mice demonstrated a lower signal for Sptbn1 mRNA (green) in RNAscope analyses as compared to osteocytes from WT littermates. Cultures were imaged with a 40X objective; scale bar in each image equals 100 μm. Images are representative of at least 3 replicates for each sex and genotype. B) Treatment with Sptbn1 siRNA significantly reduced Sptbn1 mRNA expression in MLO-Y4 osteocytes. Groups were compared with 1-way ANOVA and Fisher's LSD post-hoc tests. Bars in graphs show mean ± SEM for each group, and each black circle represents an independent biological replicate culture; bars with different superscript letters are significantly ($p<0.05$) different from one another as determined by post-hoc testing. C) Treatment of MLO-Y4 osteocytes with the thiol-oxidizing agent diamide disrupted the immunocytochemical signature for βII-spectrin. Images are representative of at least 3 replicate cultures. D-E) The maximum fluorescent intensity for D) βII-spectrin and E) F-actin (as shown by phalloidin staining) were quantified using Zen image analysis software. Groups were compared with t-tests; Bars in graphs show mean ± SEM for each group and each black circle represents one cell across three independent biological replicate experiments.

Figure 2: Osteocyte PMD formation is enhanced following Sptbn1 disruption in vitro. Treatment of MLO-Y4 osteocytes with A) diamide or B) siRNA against Sptbn1 significantly increased the number of cells with PMD, measured as cytosolic localization of 10 kDa dextran following 5 minutes of fluid shear (30 dynes/cm^2) as compared to control cultures. Representative images from each experiment are shown next to the quantitative graph. C) Primary osteocytes isolated from Sptbn1 CKO mice demonstrated a significant increase in the number of cells with cytosolic localization of dextran ($p_{genotype} = 0.0022$) following 5 minutes of fluid shear (10-50 dynes/cm^2) as compared to control cultures. A trend for an interaction effect between genotype and dextran size ($p_{genotype \times FDX} = 0.081$) suggested a tendency for larger sizes of dextran to enter Sptbn1 CKO osteocytes at a given level of loading as compared to WT cells. D) Representative images from experiments in Panel C. FDX: fluorescent dextran (3, 10, 70 kDa as indicated by the column title), DAPI (blue) = nucleus. Bars in graphs show mean ± SEM for each group and each black circle represents an independent biological replicate.

Figure 3: A) Primary osteocytes isolated from Sptbn1 CKO mice demonstrated a trend for greater FM1-43 dye influx immediately following creation of a PMD in laser wounding experiments, suggestive of increased PMD size. Bars in graph show mean +/- SEM for each group; each black circle represents an independent biological replicate experiment. B) The derivative (slopes) of the FM1-43 fluorescence versus time curves from laser wounding assays was plotted and area under the curve (AUC) quantified to measure PMD repair rate; these data suggested significantly slower rates of membrane repair in osteocytes from Sptbn1 CKO as compared to WT littermates, as seen by a significant effect of genotype in 2-factor ANOVA analyses ($p = 0.044$) for AUC. Bars in graph show mean ± SEM for each group; each black circle represents an independent biological

replicate culture.. C) Representative images from the experiments in Panels A and B, FM1-43 dye can be seen as an intracellular green fluorescent signal. A fluorescent image and a merged fluorescent + DIC (transmitted light) image is shown for each condition.

Figure 4: Sptbn1 disruption decreased post-wounding osteocyte survival. A) The combination of bead wounding and diamide treatment, but not diamide alone, promoted cell death in MLO-Y4 osteocytes as seen by increased propidium iodide (PI; red) staining. Bars in graph show mean ± SEM of independent biological replicate cultures and each black circle represents an independent biological replicate experiment; groups were compared by one-way ANOVA and Fisher's LSD post-hoc testing. Bars with different superscript letters are significantly ($p<0.05$) different from one another. FDX: 10 kDa fluorescent dextran. B) Sptbn1 knockdown by siRNA promoted increased post-wounding cell death in MLO-Y4 cells as compared to cells treated with a scrambled siRNA control. C) Primary osteocytes isolated from Sptbn1 CKO mice subjected to 5 minutes of fluid shear (30 dynes/cm^2) exhibited a nearly significant trend ($p=0.050$) for increased post-wounding cell death as compared to cells from WT mice. Bars in graphs in B and C show mean ± SEM for each group, and each black circle represents an independent biological replicate experiment.

Figure 5: Calcium signaling in Sptbn1 CKO and WT primary osteocytes initiated by laser wounding. Calcium signaling was studied via Cal-520AM fluorescence in primary osteocytes following creation of a laser-induced PMD on osteocyte dendritic processes via. A) the area under the curve (AUC) for the Cal-520 fluorescence vs. time curve and B-C) as Cal520 fluorescence in the neighboring, non-wounded osteocytes in proximity to the wounded cell. Bars in graphs A-C show mean ± SEM for each group; each black circle represents an independent biological replicate culture. D) Representative images from the experiments shown in graphs A-C, captured at -1 seconds before wounding, 0 seconds (i.e., at the time of wounding), and 30 seconds after wounding.

Figure 6: PMD formation from voluntary wheel running and uniaxial tibial loading. A) Osteocyte PMD were detected via immunohistochemical staining to detect cytosolic endogenous mouse albumin in tibias from male and female Control and High Runner mice that were either given access to a voluntary running wheel (wheel access: yes) or not provided access to a running wheel (wheel access: no) for 6 days prior to sacrifice. Wheel access increased PMD abundance. Bars in graphs show mean ± SEM for each group; each black circle represents one mouse. Groups were compared with 3-way ANOVA with 2-way interaction effects. B) Representative images showing endogenous albumin (green) staining in tibias from male and female Control and High Runner mice with or without access to a running wheel quantified in Panel A. C) Osteocyte PMD were detected via immunohistochemical staining to detect cytosolic endogenous mouse albumin in tibias from female CD-1 mice subjected to a single bout of uniaxial tibial loading. Bars in graphs show mean ± SEM for each limb; each black circle represents one mouse. Left vs. right sides were

compared for each mouse using paired t-tests. D) Representative images showing endogenous albumin (green) staining in osteocytes in tibial sections from CD-1 mice exposed to a single bout of uniaxial loading quantified in Panel C.

Figure 7: Blunted increase in cortical bone thickness with uniaxial tibial loading in Sptbn1 CKO mice. A) Micro-computed tomography was used to measure cortical bone thickness in the left and right tibia of each mouse. The percent difference in cortical thickness between the loaded and non-loaded limb was calculated for each mouse as: % difference Ct.Th = [Ct.Th left tibia – Ct.Th right tibia] / Ct.Th right tibia. The relative increase in Ct.Th for the loaded left limb was blunted in Sptbn1 CKO mice, shown by a significant effect of genotype in 2-way ANOVA ($p=0.0153$). Boxes in the graph show median, quartiles and outlier fences for each dataset. Each data point (black circle) represents one mouse. B) Paired t-tests were also used to compare cortical bone thickness between the loaded left limb and the non-loaded right limb for each Sptbn1 CKO and WT mouse. Uniaxial tibial loading induced a significant increase in Ct.Th, shown by a significant p-value for paired t-tests ($p=0.0025$), and when grouped by genotype, the Sptbn1 CKO mice showed a lower relative increase in Ct.Th as compared to the WT animals ($p=0.0101$). Bars in graphs B show mean ± SEM for each group, and each symbol shown represents the left (L) and right (R) tibia from one mouse. C) Representative microCT reconstructions for samples shown in Panel A.

Figure 8: A) Although PMD were increased by acute loading (p paired t-test left vs. right <0.0001; not shown), the relative difference in PMD abundance between the loaded left limb and non-loaded right limb was not different between Sptbn1 CKO and WT mice ($p_{genotype} = 0.5506$). Bars in graph show mean ± SEM for each group; each black circle represents one mouse. B) Representative images showing endogenous albumin quantified in panel A. C-F) Osteocyte lacunae vacancy in Sptbn1 CKO and WT mice subjected to acute or chronic uniaxial tibial loading. The relative number of empty osteocyte lacunae normalized to the total number of osteocyte lacunae was quantified in longitudinal sections loaded left tibias stained with Goldner's Trichrome. While no differences in the relative abundance of empty osteocyte lacunae were observed in mice subjected to one acute tibial loading bout (C-D; $p=0.8596$), both male and female Sptbn1 CKO mice showed more empty lacunae after 2 weeks of chronic loading (E-F; 6 loading bouts), as shown by a significant effect of genotype in 2-way ANOVA ($p=0.0102$). Bars in graph show mean ± SEM for each group; each black circle represents one mouse.

SUPPLEMENTAL FIGURES / TABLES

Supplemental Figure 1: A) Bone mineral density in High Runner and control mice. Bone mineral density (BMD) was measured in the tibial mid-diaphysis by dual energy x-ray absorptiometry. Bars in graph show mean ± SEM for each group; each black circle represents

one mouse. Wheel access was associated with lower tibial BMD as shown by a significant effect of selection (p=0.0457). B) Representative images from the femoral mid-diaphysis showing cortical bone calcein labeling in High Runner and control mice**.**

Supplemental Figure 2: Cortical bone geometry and dynamic histomorphometry in female CD-1 mice subjected to uniaxial tibial loading. Female CD-1 mice were subjected to 2 weeks of uniaxial tibial loading beginning at 12 weeks of age. Bone properties in the left (loaded) versus right (non-loaded) tibia were compared for each mouse via paired t-tests. Micro-computed tomography was used to measure cortical bone thickness (A) and cortical bone area (B). A subset of tibias was prepared for dynamic histomorphometric analysis of calcein labels, measuring periosteal and endocortical mineral apposition rates (C-D) and periosteal and endocortical mineralizing surfaces (E-F). Representative images are shown at low magnification in Panel G and at higher magnification in Panel H. Bars in graphs show mean ± SEM for each group; each black circle represents one mouse.

Supplemental Figure 3: Cortical bone geometry in the non-loaded right limb of Sptbn1 CKO and WT mice at 14 weeks of age. Micro-computed tomography was used to measure cortical bone area **(A)** and cortical bone thickness **(B)** in the right (non-loaded) tibia of each mouse. Bars in graphs show mean ± SEM for each group; each black circle represents one mouse.

Supplemental Figure 4: Cortical bone geometry and dynamic histomorphometry in Sptbn1 CKO and WT mice subjected to uniaxial tibial loading. Sptbn1 CKO and WT littermate mice were subjected to 2 weeks of uniaxial tibial loading beginning at 12 weeks of age. The percent difference in bone properties between the left (loaded) versus right (non-loaded) tibia was compared between male and female Sptbn1 CKO and WT mice with 2-way ANOVA, and the matched pairs comparison of bone properties between the left versus right tibia for each mouse was analyzed via paired t-tests with grouping by genotype for cortical bone area (**A-B**), periosteal mineralizing surface and mineral apposition rate (**C-E**), and endocortical mineralizing surface and mineral apposition rate (**F-H**). Percent difference was not calculated for mineral apposition rates due to an appreciable number of non-loaded right tibias lacking double labeled surface. Bars in graphs show mean ± SEM for each group. Each black circle (panels **A,C,F**) or letter (panels **B,D,E,G,H**) in graphs represents one mouse; L: left/loaded, R: right/non-loaded for pairwise comparison graphs.

Supplemental Table 1A: Cortical bone architectural properties in the mid-diaphysis of the femur for Control and High Runner mice.

Sex	Selection	n	Wheel	Ct.B.Ar (mm^2)			Ct.Th (mm)		
Female	Control (line 2)	4	no	1.185	±	0.067	0.262	±	0.015
Female	Control (line 2)	6	yes	1.172	±	0.101	0.261	±	0.018
Female	High Runner (line 8)	6	no	1.251	±	0.095	0.245	±	0.014
Female	High Runner (line 8)	6	yes	1.174	±	0.091	0.250	±	0.018
Male	Control (line 2)	5	no	1.251	±	0.133	0.268	±	0.031
Male	Control (line 2)	6	yes	1.223	±	0.099	0.251	±	0.013
Male	High Runner (line 8)	6	no	1.354	±	0.151	0.261	±	0.026
Male	High Runner (line 8)	6	yes	1.374	±	0.104	0.265	±	0.011

P-values			
	Wheel	0.4593	0.6651
	Selection	**0.0185**	0.3776
	Sex	**0.0027**	0.2410
	Wheel x Selection	0.9002	0.2707
	Wheel x Sex	0.5388	0.4386
	Selection x Sex	0.1652	0.1416
	Wheel x Selection x Sex	0.3931	0.5241

Means +/- SEM for each group are shown. Wheel: yes = granted wheel access for 6 days prior to sacrifice, no = no wheel access. Selection: High Runner = mice from lines selectively bred to have high voluntary wheel running activity, Control = mice from non-selected control lines. Ct.B.Ar = cortical bone area, Ct.Th = cortical bone thickness

Supplemental Table 1B: Cortical bone dynamic histomorphometry properties in the mid-diaphysis of the femur for Control and High Runner mice.

Sex	Selection	n	Wheel	Ec. MS/BS (%)	Ec.MAR (um/day)	Ps.MS/BS (%)	Ps.MAR (um/day)
Female	Control	16	no	0.497 ± 0.048	0.848 ± 0.043	0.300 ± 0.029	0.831 ± 0.042
Female	Control	16	yes	0.515 ± 0.040	0.876 ± 0.055	0.376 ± 0.034	1.007 ± 0.069
Female	High Runner	13	no	0.382 ± 0.049	0.835 ± 0.057	0.310 ± 0.040	0.827 ± 0.082
Female	High Runner	15	yes	0.384 ± 0.040	0.849 ± 0.064	0.258 ± 0.019	0.841 ± 0.038
Male	Control	12	no	0.381 ± 0.052	0.774 ± 0.060	0.315 ± 0.044	0.813 ± 0.105
Male	Control	15	yes	0.293 ± 0.057	0.656 ± 0.091	0.364 ± 0.019	1.008 ± 0.057
Male	High Runner	13	no	0.306 ± 0.047	0.830 ± 0.063	0.317 ± 0.023	0.893 ± 0.061
Male	High Runner	13	yes	0.205 ± 0.044	0.648 ± 0.106	0.264 ± 0.029	0.873 ± 0.065

P-values	Wheel	0.1864	0.2654	0.9291	0.4985
	Selection	**0.0100**	0.1236	0.9412	0.7589
	Sex	**0.0312**	0.9794	0.1466	0.5692
	Mini	***0.0713***	0.7003	0.6809	0.3594
	Wheel x Selection	0.1846	0.1281	0.8101	0.8679
	Wheel x Sex	0.6165	0.7067	***0.0540***	0.6570
	Selection x Sex	0.7021	0.6773	0.8892	0.3875
	Wheel x Selection x Sex	0.9747	0.7536	0.8092	0.7040

Means +/- SEM for each group are shown. Wheel: yes = granted wheel access for 6 days prior to sacrifice, no = no wheel access. Selection: High Runner = mice from lines selectively bred to have high voluntary wheel running activity, Control = mice from non-selected control lines. Ec. = endocortical, Ps. = periosteal, MS/BS = mineralizing surface, MAR = mineral apposition rate.

Supplemental Table 2: Summary of mixed models SAS statistical analyses of Control and High Runner mice

(please see spreadsheet)

Supplemental Table 3: Dual energy x-ray absorptiometry (DXA) measurements of Sptbn1 CKO and WT littermate mice at various ages.

							P-values		
Age	**Sex**	**Genotype**	**n**	**Whole Body BMD (g/cm^2)**			**Genotype**	**Sex**	**Genotype x Sex**
1 month	Female	WT	9	0.148	±	0.002			
	Female	CKO	3	0.145	±	0.002	0.807	0.408	0.195
	Male	WT	14	0.147	±	0.002			
	Male	CKO	6	0.151	±	0.004			
5 months	Female	WT	10	0.218	±	0.008			
	Female	CKO	5	0.216	±	0.010	0.238	**0.003**	0.375
	Male	WT	17	0.201	±	0.005			
	Male	CKO	10	0.185	±	0.008			

Means +/- SEM for each group are shown. BMD = bone mineral density

Supplemental Table 4: Cortical bone geometrical properties in the mid-diaphysis of the femur for Sptbn1 CKO and WT mice at 5 months of age

Genotype	Sex	n	Ct.B.Ar (mm^2)		Ipolar (mm^4)		Imax (mm^4)		Imin (mm^4)		Ct.Th (mm)	
WT	Male	3	0.858	± 0.055	0.422	± 0.096	0.280	± 0.062	0.142	± 0.034	0.180	± 0.013
CKO	Male	4	0.881	± 0.136	0.503	± 0.137	0.326	± 0.087	0.177	± 0.054	0.172	± 0.014
			p-value (CKO vs. WT)	0.799	p-value (CKO vs. WT)	0.4239	p-value (CKO vs. WT)	0.474	p-value (CKO vs. WT)	0.374	p-value (CKO vs. WT)	0.4595

Means +/- SEM for each group are shown. Ct.B.Ar = cortical bone area, Ipolar = polar moment of inertia, Imax = maximum moment of inertia, Imin =minimum moment of inertia, Ct.Th = cortical bone thickness.

Supplemental Table 5: Cortical bone geometrical properties in the tibial mid-diaphysis of Sptbn1 CKO and WT after 2 weeks of mechanical loading.

Sex	Genotype	Side	n	B.Ar (mm^2)		SE	Ipolar (mm^4)		SE	Imax (mm^4)		SE	Imin (mm^4)		SE	Ct.Th (mm)		SE
Female	WT	Left (loaded)	14	0.799	±	0.027	0.366	±	0.026	0.271	±	0.019	0.095	±	0.007	0.146	±	0.007
Female	WT	Right (non-loaded)	14	0.682	±	0.035	0.307	±	0.025	0.235	±	0.019	0.072	±	0.007	0.131	±	0.006
		Paired t-test:		**<0.0001**			**<0.0001**			**0.0003**			**<0.0001**			**0.0016**		
Female	CKO	Left (loaded)	8	0.779	±	0.017	0.316	±	0.018	0.232	±	0.012	0.084	±	0.007	0.142	±	0.007
Female	CKO	Right (non-loaded)	8	0.656	±	0.017	0.257	±	0.015	0.195	±	0.011	0.062	±	0.005	0.134	±	0.006
		Paired t-test		**0.0001**			**0.0011**			**0.0034**			**0.0007**			0.1286		
Male	WT	Left (loaded)	18	0.908	±	0.017	0.537	±	0.024	0.413	±	0.020	0.124	±	0.005	0.142	±	0.005
Male	WT	Right (non-loaded)	18	0.858	±	0.022	0.495	±	0.026	0.372	±	0.020	0.122	±	0.007	0.135	±	0.005
		Paired t-test		**0.0006**			**0.0040**			**0.0008**			0.6922			***0.0556***		
Male	CKO	Left (loaded)	11	0.846	±	0.029	0.455	±	0.035	0.341	±	0.026	0.115	±	0.010	0.137	±	0.006
Male	CKO	Right (non-loaded)	11	0.824	±	0.029	0.419	±	0.030	0.308	±	0.022	0.111	±	0.009	0.143	±	0.006
		Paired t-test		0.2652			**0.0452**			**0.0300**			0.3434			**0.0256**		

Means +/- SEM for each group are shown. Ct.B.Ar = cortical bone area, Ipolar = polar moment of inertia, Imax = maximum moment of inertia, Imin =minimum moment of inertia, Ct.Th = cortical bone thickness.

Figure 1

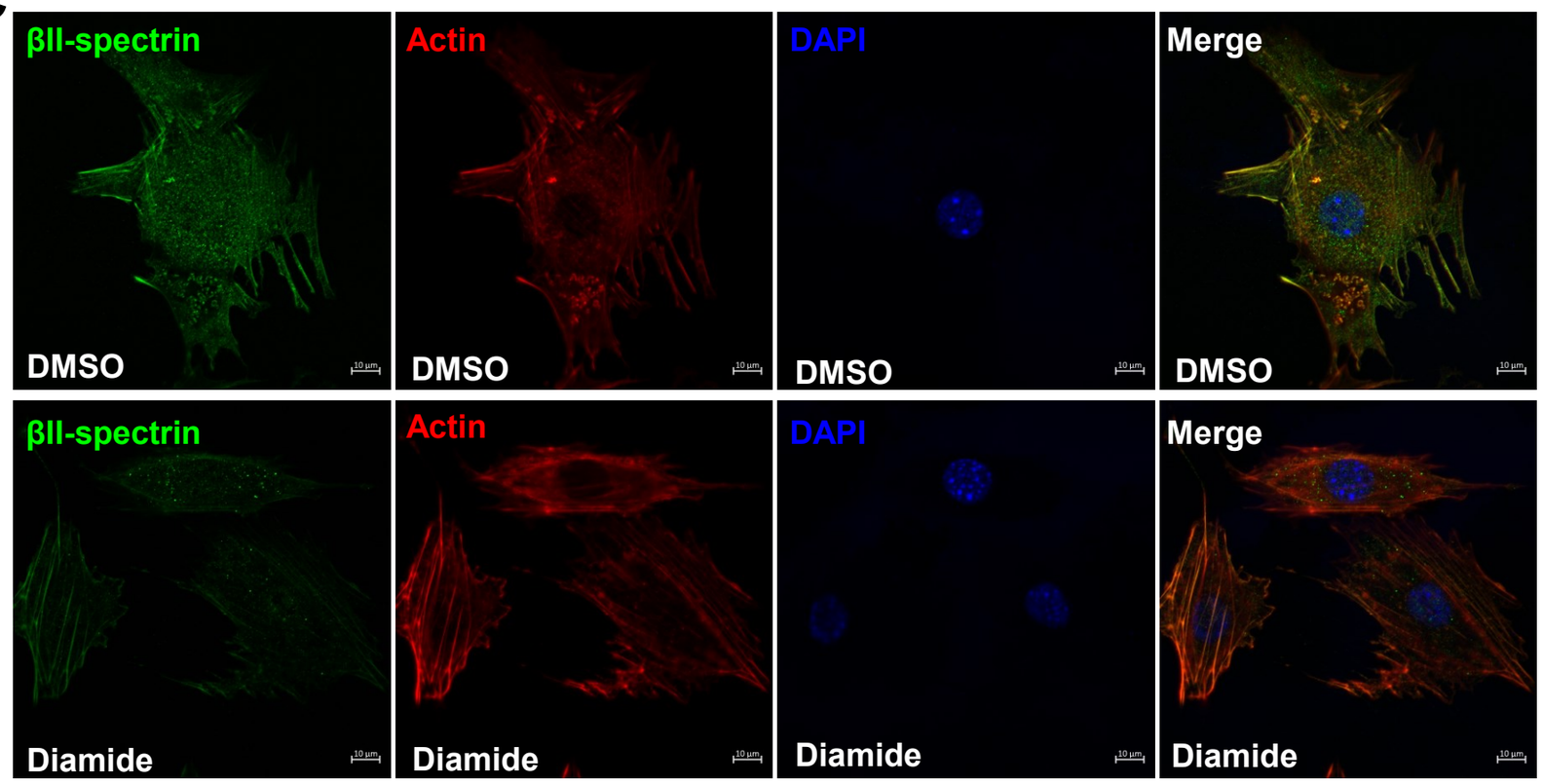

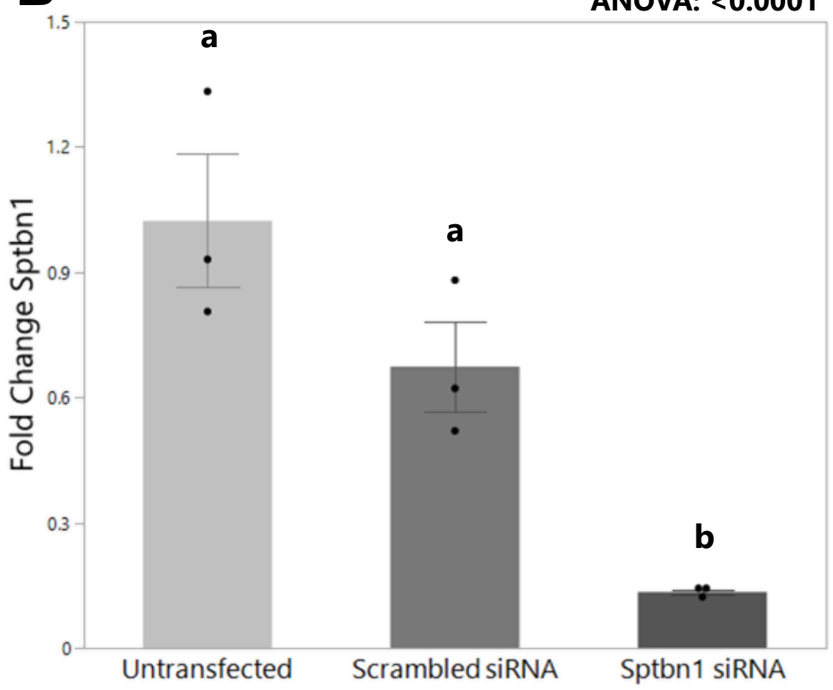

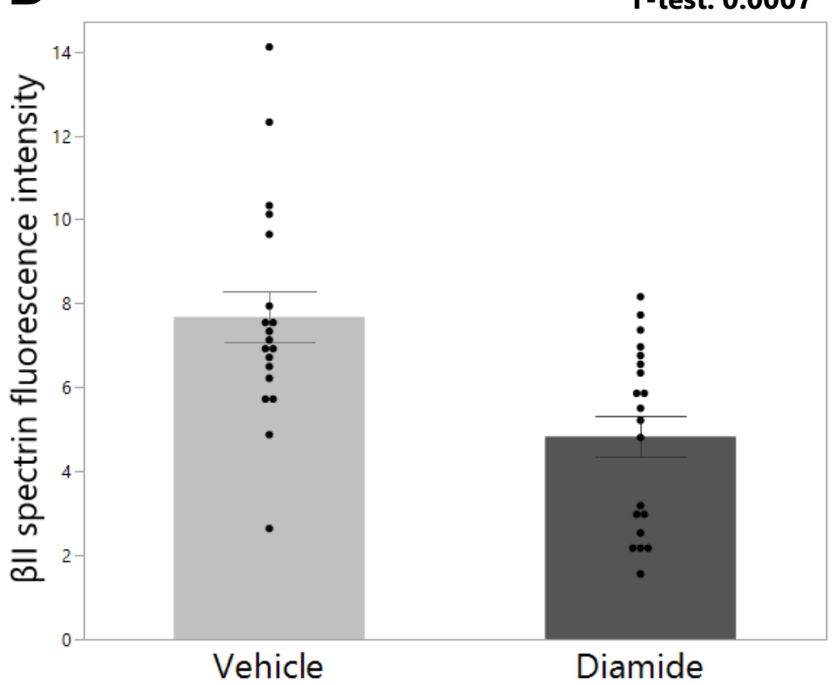

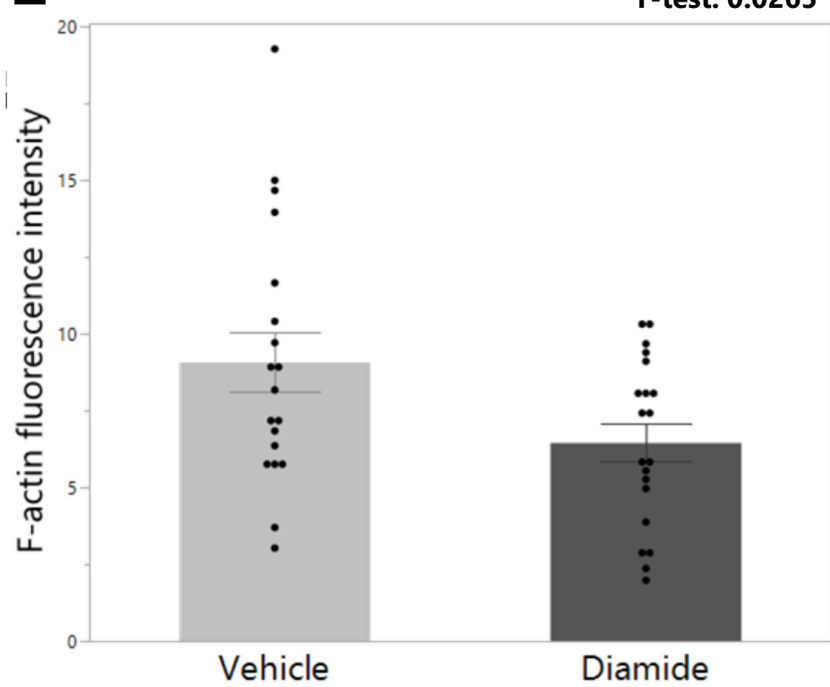

Figure 1: Validation of Sptbn1 disrupting strategies for in vitro studies. A) Primary osteocytes isolated from male and female Sptbn1 CKO mice demonstrated a lower signal for Sptbn1 mRNA (green) in RNAscope analyses as compared to osteocytes from WT littermates. Cultures were imaged with a 40X objective; scale bar in each image equals 100 µm. Images are representative of at least 3 replicates for each sex and genotype. B) Treatment with Sptbn1 siRNA significantly reduced Sptbn1 mRNA expression in MLO-Y4 osteocytes. Groups were compared with 1-way ANOVA and Fisher's LSD post-hoc tests. Bars shown mean +/- SEM for each group, and each dot represents an independent biological replicate culture; bars with different superscript letters are significantly ($p<0.05$) different from one another as determined by post-hoc testing. C) Treatment of MLO-Y4 osteocytes with the thiol-oxidizing agent diamide disrupted the immunocytochemical signature for βII-spectrin. Images are representative of at least 3 replicate cultures. D-E) The maximum fluorescent intensity for D) βII-spectrin and E) actin (as shown by phalloidin staining) were quantified using Zen image analysis software. Groups were compared with t-tests; each dot represents one cell across three independent biological replicate experiments.

Figure 2

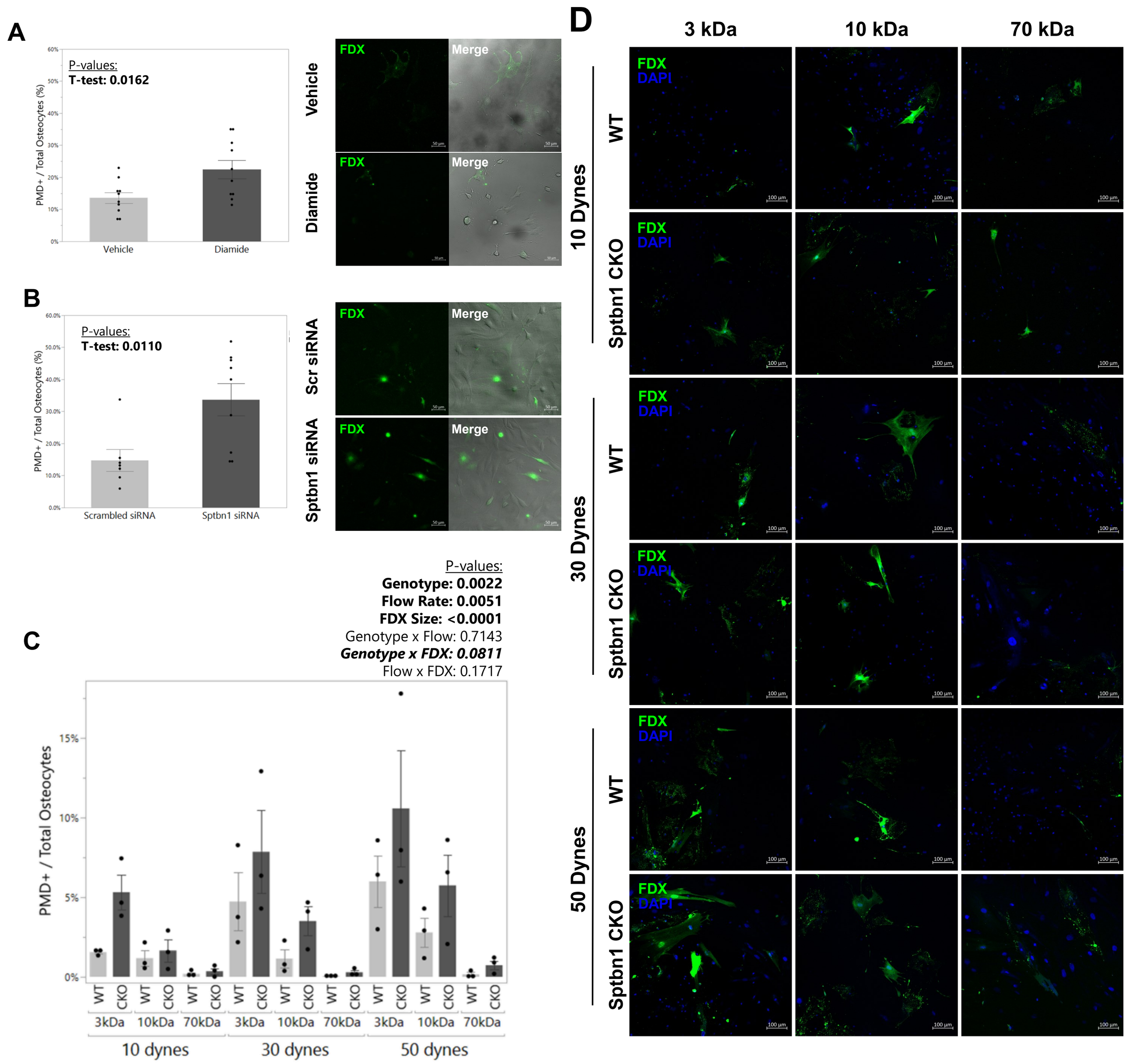

Figure 2: Osteocyte PMD formation is enhanced following Sptbn1 disruption in vitro. Treatment of MLO-Y4 osteocytes with A) diamide or B) siRNA against Sptbn1 significantly increased the number of cells with PMD, measured as cytosolic localization of 10 kDa dextran following 5 minutes of fluid shear (30 dynes/cm^2) as compared to control cultures. Representative images from each experiment are shown next to the quantitative graph. C) Primary osteocytes isolated from Sptbn1 CKO mice demonstrated a significant increase in the number of cells with cytosolic localization of dextran (pgenotype = 0.0022) following 5 minutes of fluid shear (10-50 dynes/cm^2) as compared to control cultures. A trend for an interaction effect between genotype and dextran size (pgenotype x FDX = 0.081) suggested a tendency for larger sizes of dextran to enter Sptbn1 CKO osteocytes at a given level of loading as compared to WT cells. D) Representative images from experiments in Panel C. FDX: fluorescent dextran (3, 10, 70 kDa as indicated by the column title), DAPI = nucleus.

Figure 3

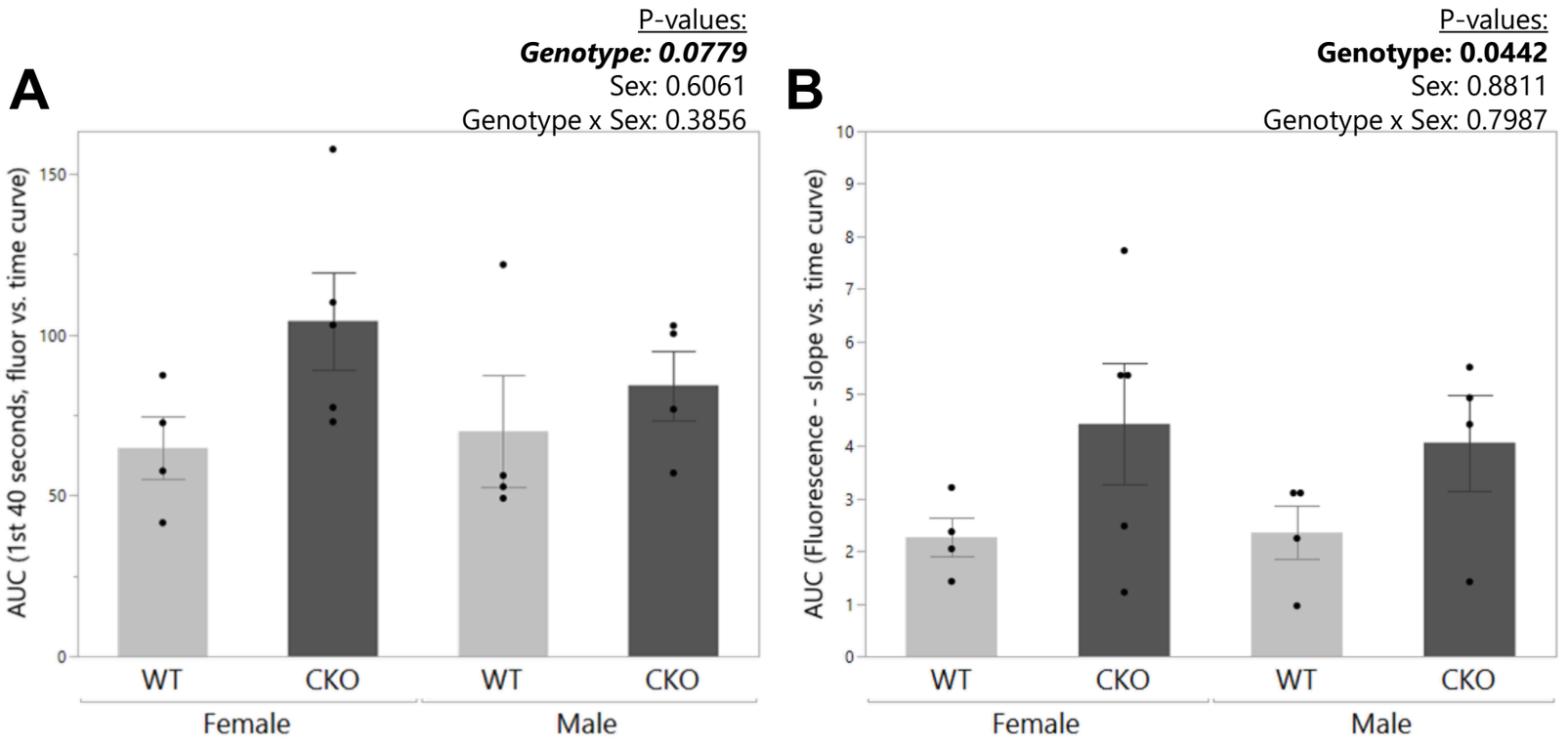

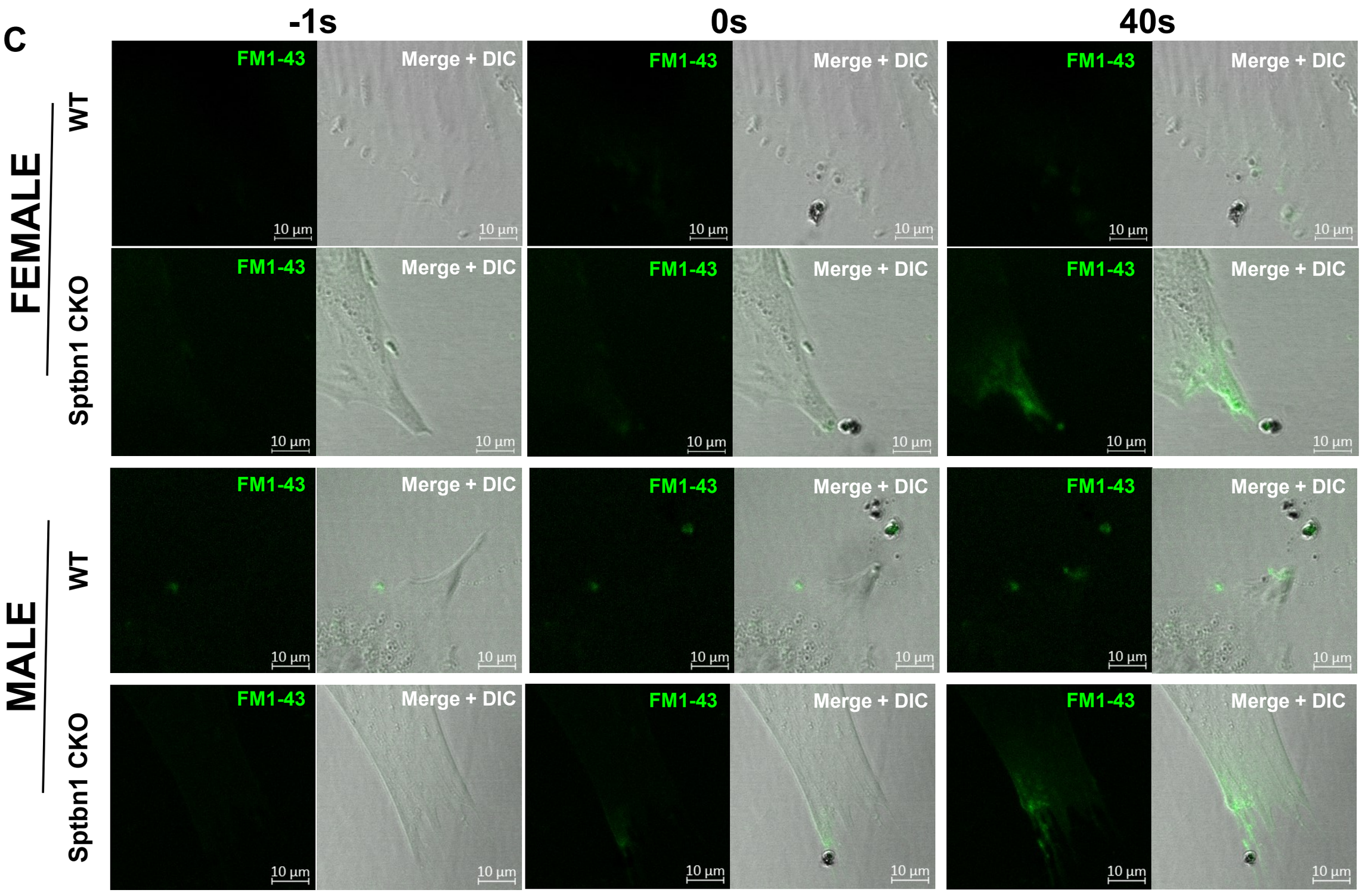

Figure 3: A) Primary osteocytes isolated from Sptbn1 CKO mice demonstrated a trend for greater FM1-43 dye influx immediately following creation of a PMD in laser wounding experiments, suggestive of increased PMD size. Bars show mean +/- SEM for each group; each dot represents an independent biological replicate experiment. B) The derivative (slopes) of the FM1-43 fluorescence versus time curves from laser wounding assays was plotted and area under the curve (AUC) quantified to measure PMD repair rate; these data suggested significantly slower rates of membrane repair in osteocytes from Sptbn1 CKO as compared to WT littermates, as seen by a significant effect of genotype in 2-factor ANOVA analyses (p =0 .044) for AUC. Bars show mean +/- SEM for each group; each dot represents an independent biological replicate culture.. C) Representative images from the experiments in Panels A and B, FM1-43 dye can be seen as the intracellular green fluorescent signal. A fluorescent image and a merged fluorescent + DIC (transmitted light) image is shown for each condition.

Figure 4

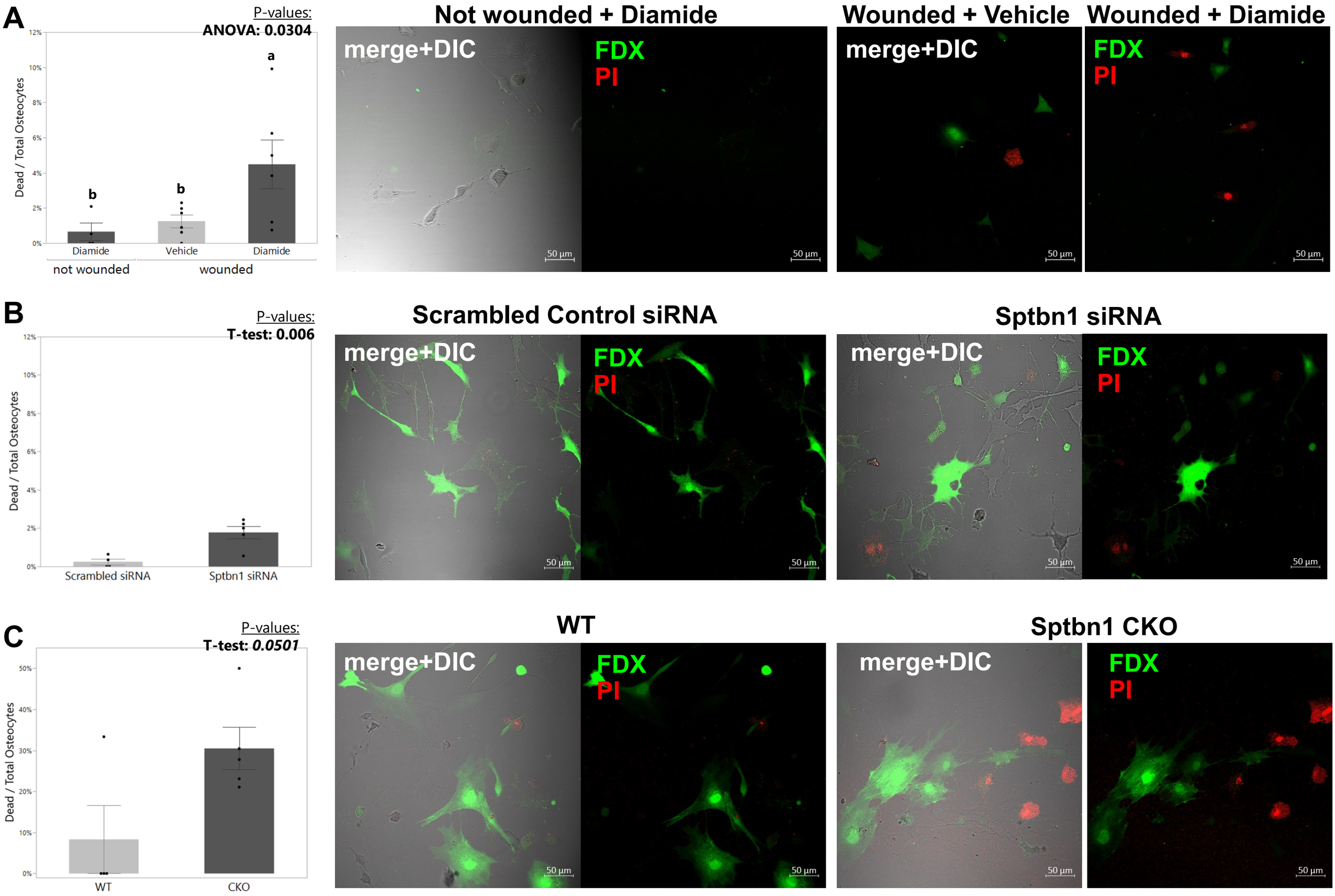

Figure 4: Sptbn1 disruption decreased post-wounding osteocyte survival. A) The combination of bead wounding and diamide treatment, but not diamide alone, promoted cell death in MLO-Y4 osteocytes as seen by increased propidium iodide (PI; red) staining. Bars show mean +/- SEM of independent biological replicate cultures; groups were compared by one-way ANOVA and Fisher's LSD post-hoc testing. Bars with different superscript letters are significantly ($p<0.05$) different from one another. FDX: 10 kDa fluorescent dextran. B) Sptbn1 knockdown by siRNA promoted increased post-wounding cell death in MLO-Y4 cells as compared to cells treated with a scrambled siRNA control. C) Primary osteocytes isolated from Sptbn1 CKO mice subjected to 5 minutes of fluid shear (30 dynes/cm^2) exhibited a nearly significant trend ($p=0.050$) for increased post-wounding cell death as compared to cells from WT mice. Bars show mean +/- SEM for each group, and each dot represents an independent biological replicate experiment.

Figure 5

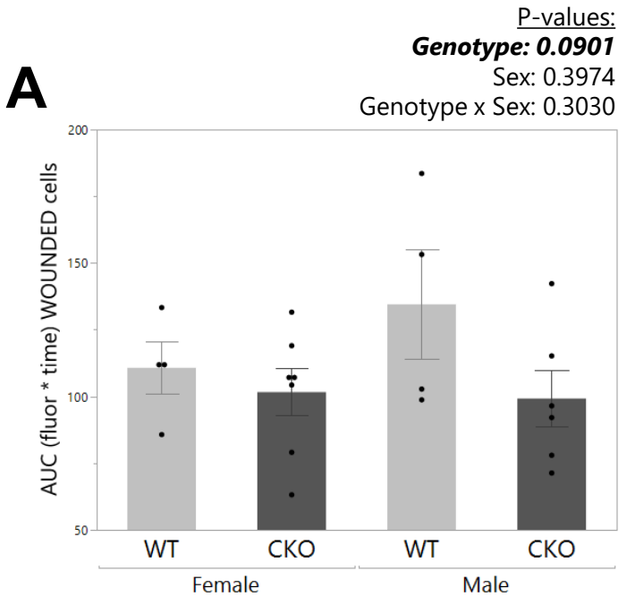

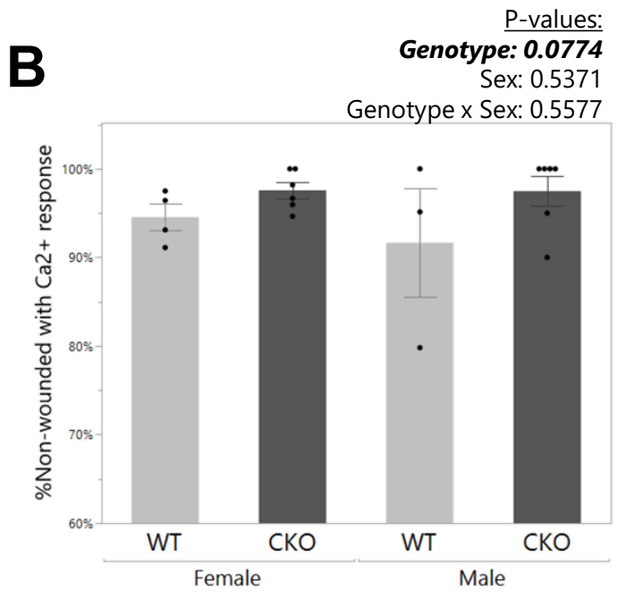

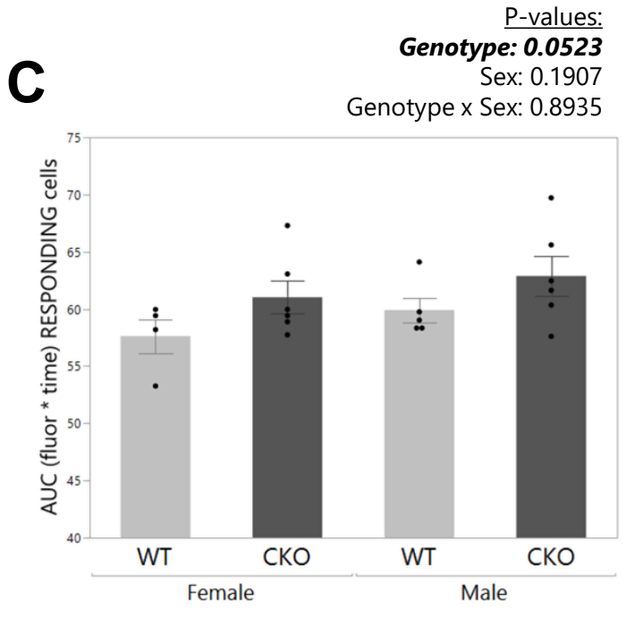

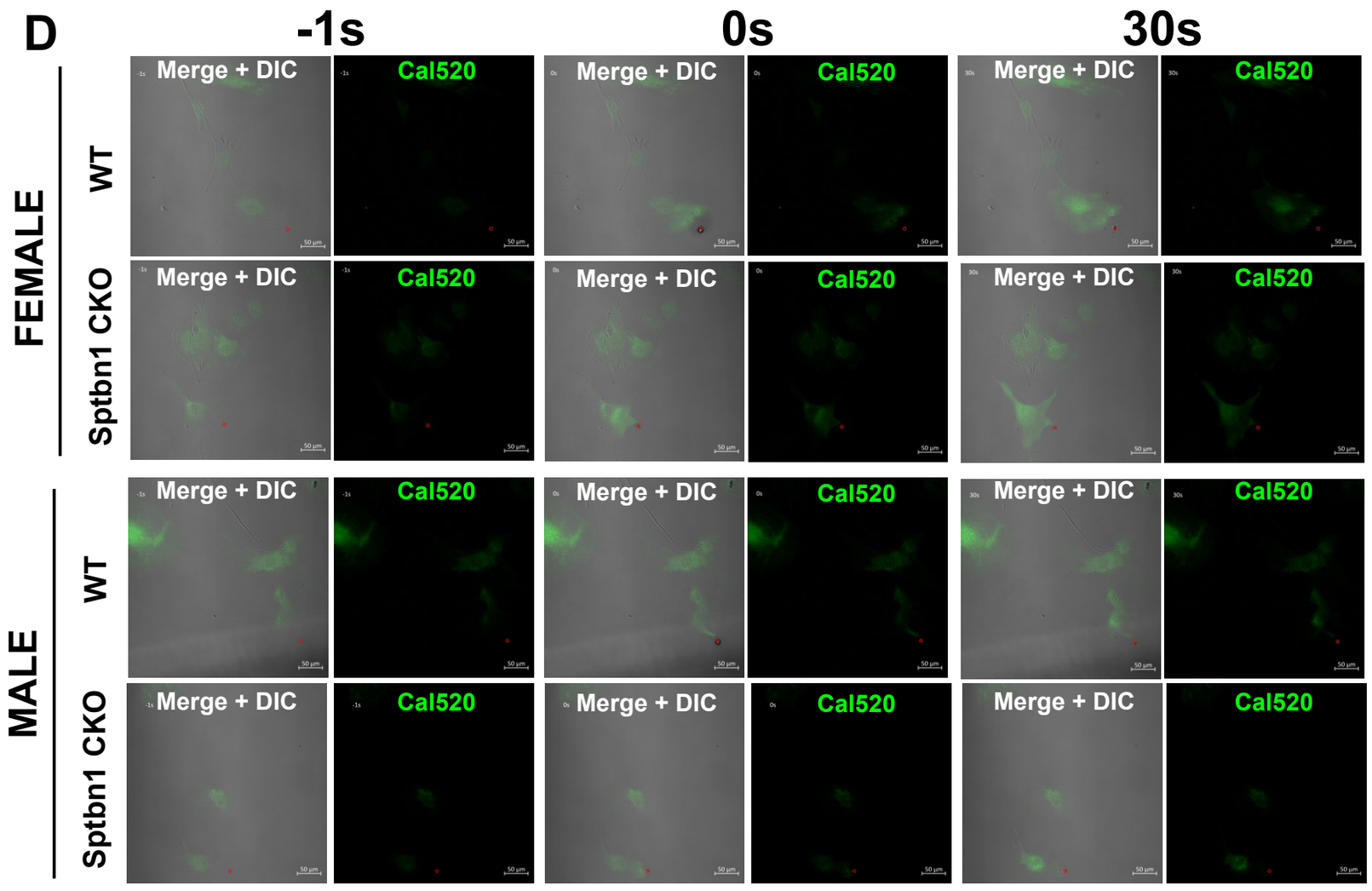

Figure 5: Calcium signaling in Sptbn1 CKO and WT primary osteocytes initiated by laser wounding. Calcium signaling was studied via Cal-520AM fluorescence in primary osteocytes following creation of a laser-induced PMD on osteocyte dendritic processes. A) The area under the curve (AUC) for the Cal-520 fluorescence vs. time curve tended to be reduced in the wounded Sptbn1 CKO as compared to WT osteocytes, as shown by a trend for an effect of genotype in 2-way ANOVA analyses (p=0.090). B-C) Cal520 fluorescence was also monitored in the neighboring, non-wounded osteocytes in proximity to the wounded cell. The Sptbn1 CKO cultures tended to show B) more cells with Cal520 fluorescence signals rising above baseline, as shown by a trend for an effect of genotype in 2-way ANOVA analyses (p=0.077). Consistent with this idea, C) the AUC for the Cal520 fluorescence vs. time curve in these non-wounded neighboring osteocytes tended to be increased in the CKO cultures, shown by a trend for an effect of genotype in 2-way ANOVA analyses (p=0.052). Bars shown mean +/- SEM for each group; each dot represents an independent biological replicate culture. D) Representative images from the experiments shown in Panels A-C, captured at -1 seconds before wounding, 0 seconds (i.e., at the time of wounding), and 30 seconds after wounding.

Figure 6

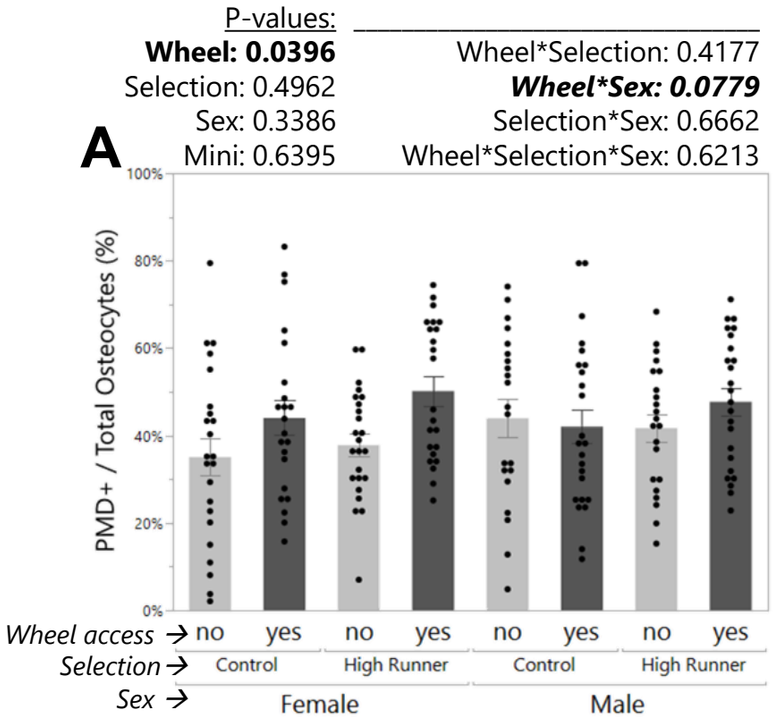

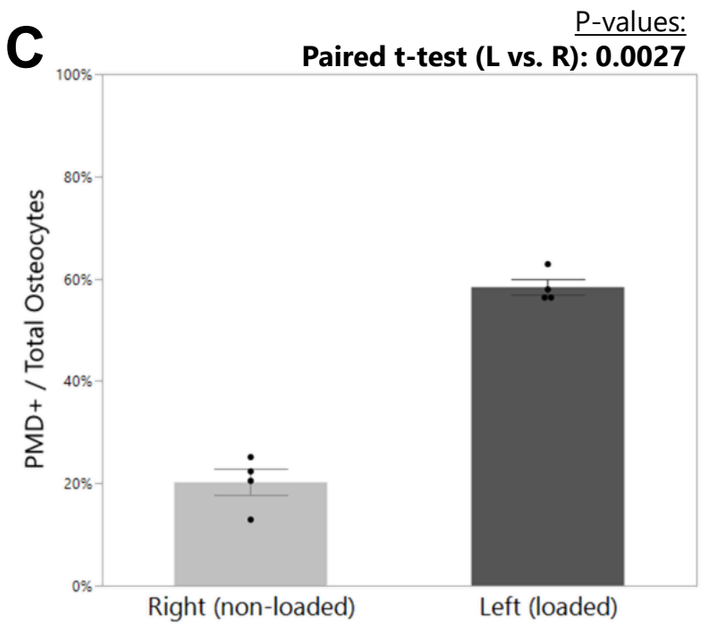

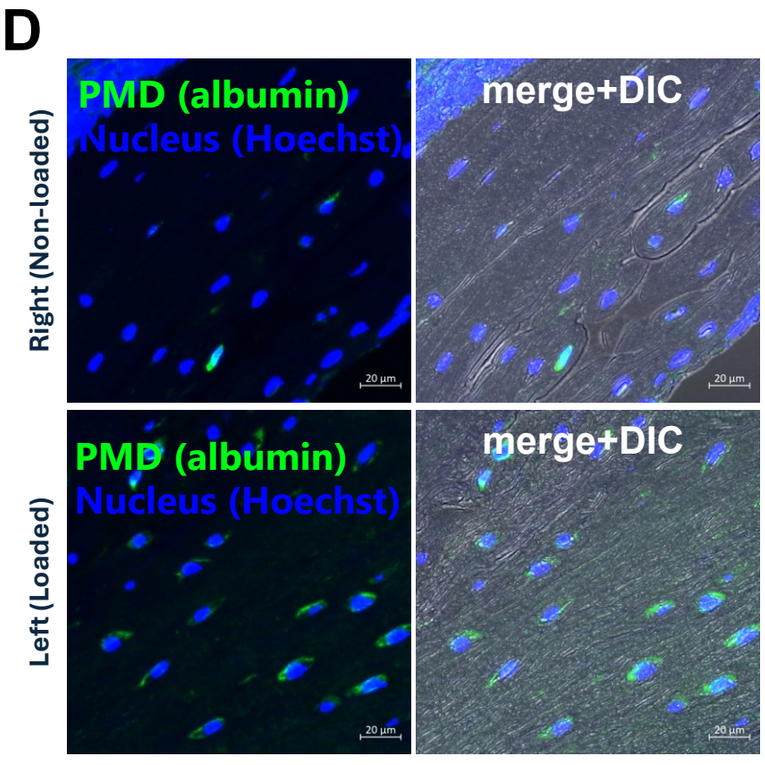

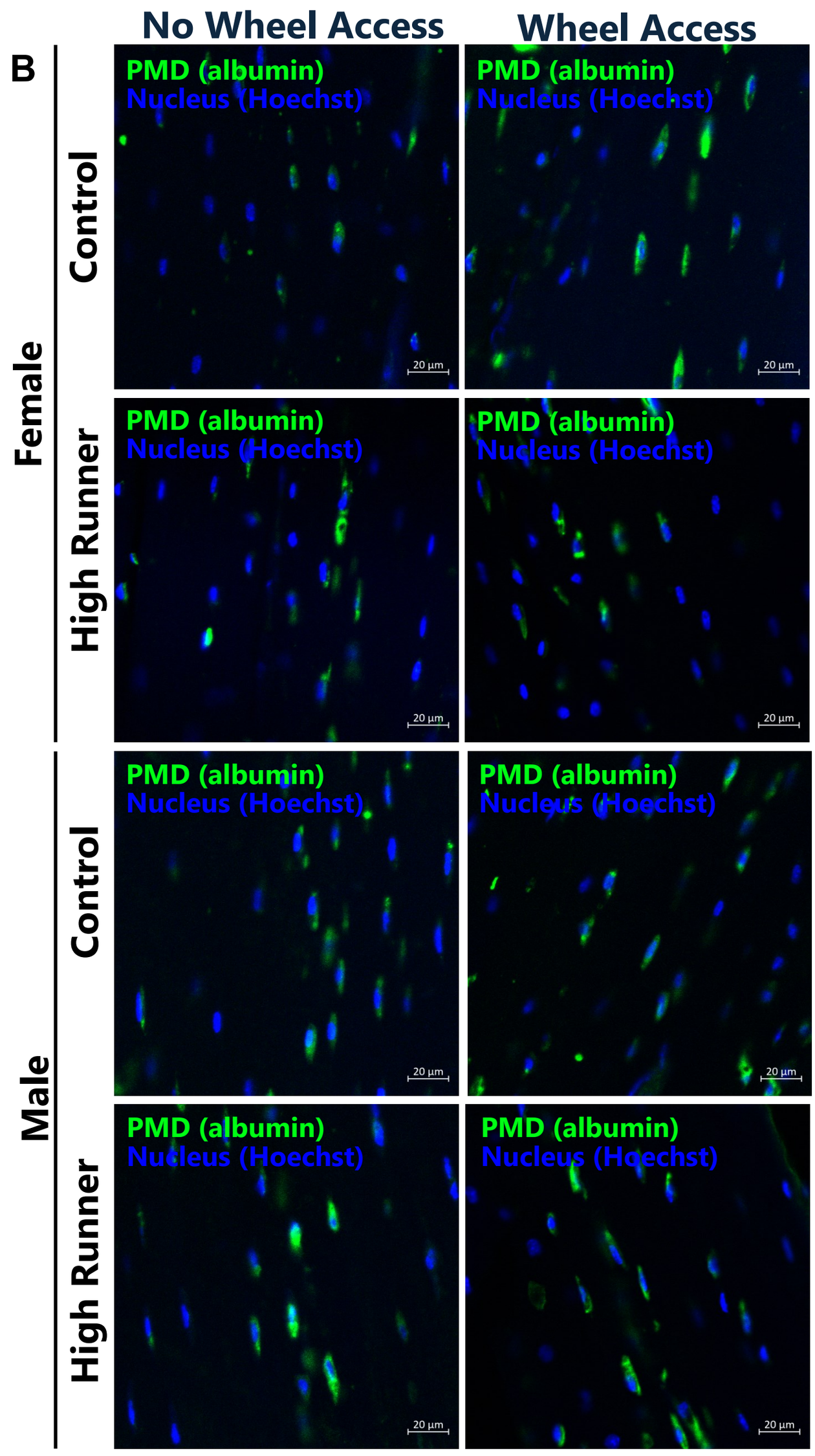

Figure 6: PMD formation from voluntary wheel running and uniaxial tibial loading. A) Osteocyte PMD were detected via immunohistochemical staining to detect cytosolic endogenous mouse albumin in tibias from male and female Control and High Runner mice that were either given access to a voluntary running wheel (wheel access: yes) or not provided access to a running wheel (wheel access: no) for 6 days prior to sacrifice. Bars show mean +/- SEM for each group; each dot represents one mouse. Groups were compared with 3-way ANOVA with 2-way interaction effects. B) Representative images showing endogenous albumin (green) staining in tibias from male and female Control and High Runner mice with or without access to a running wheel quantified in Panel A. C) Osteocyte PMD were detected via immunohistochemical staining to detect cytosolic endogenous mouse albumin in tibias from female CD-1 mice subjected to a single bout of uniaxial tibial loading. Bars show mean +/- SEM for each limb; each dot represents one mouse. Left vs. right sides were compared for each mouse using paired t-tests. D) Representative images showing endogenous albumin (green) staining in osteocytes in tibial sections from CD-1 mice exposed to a single bout of uniaxial loading quantified in Panel C.

Figure 7

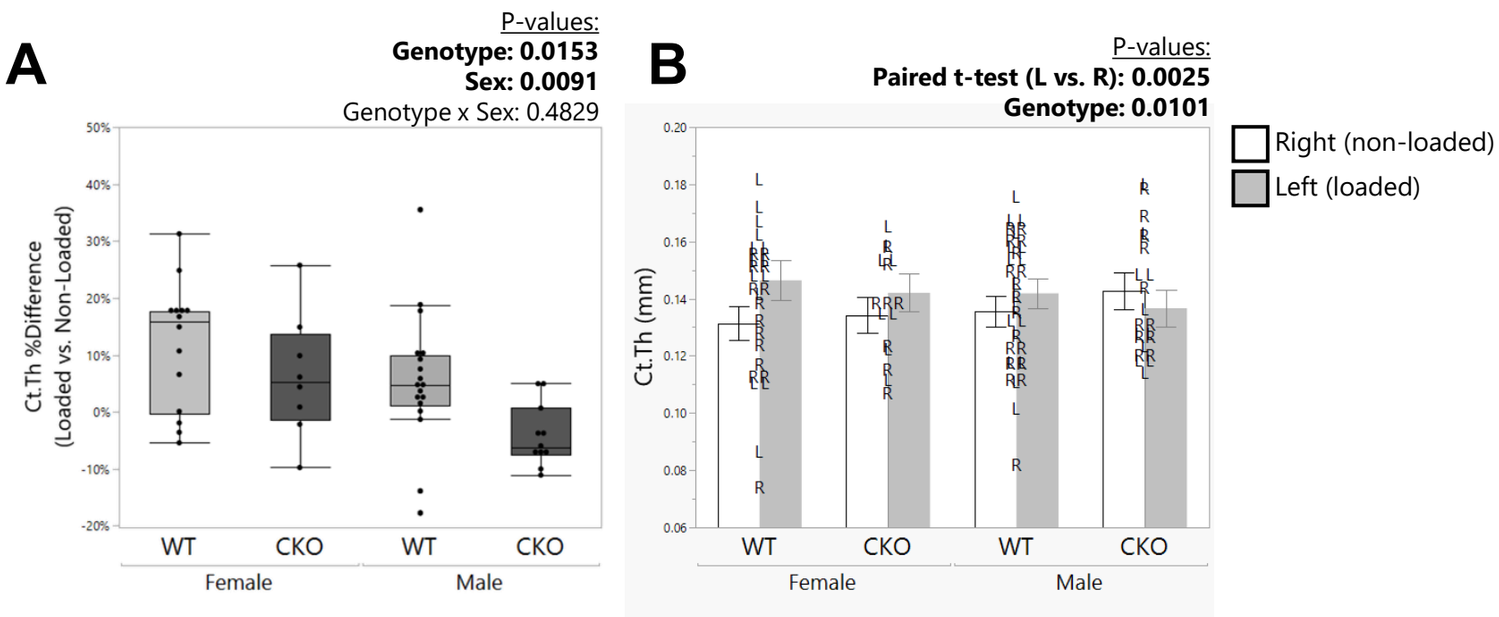

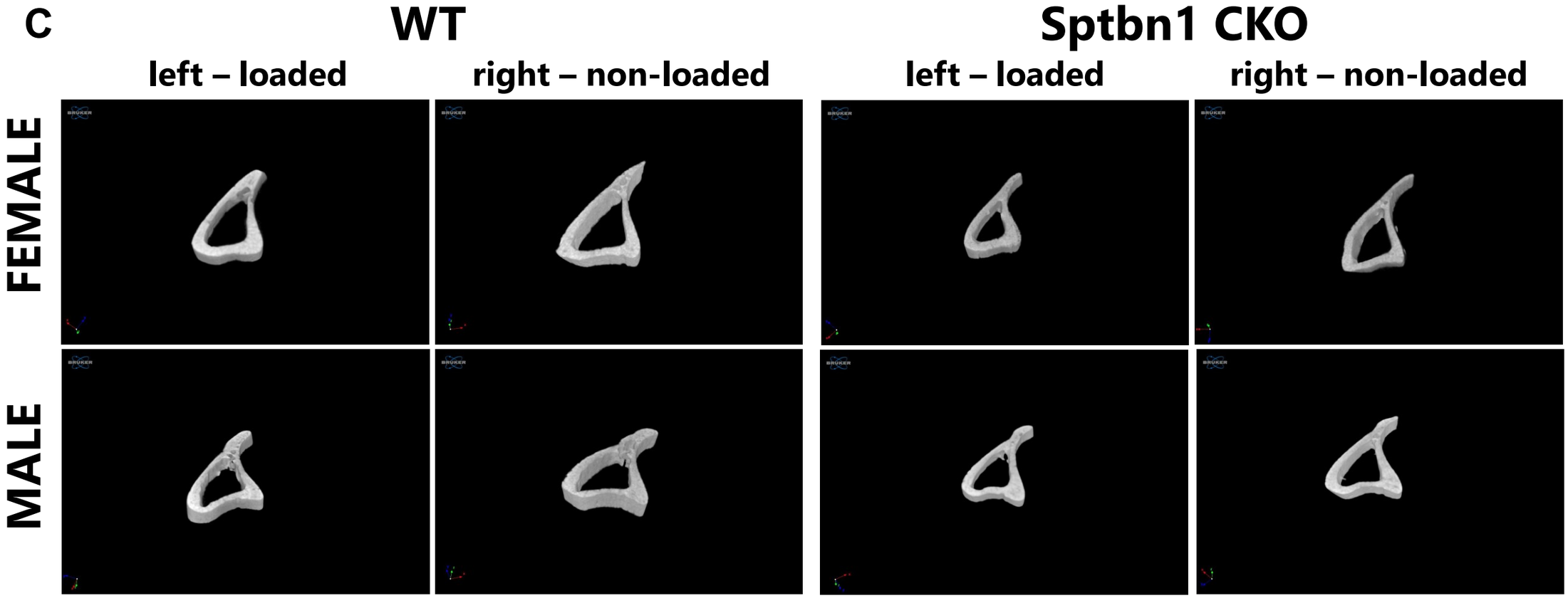

Figure 7: Blunted increase in cortical bone thickness with uniaxial tibial loading in Sptbn1 CKO mice. A) Micro-computed tomography was used to measure cortical bone thickness in the left and right tibia of each mouse. The percent difference in cortical thickness between the loaded and non-loaded limb was calculated for each mouse as: % difference Ct.Th = [Ct.Th left tibia – Ct.Th right tibia] / Ct.Th right tibia. The relative increase in Ct.Th for the loaded left limb was blunted in Sptbn1 CKO mice, shown by a significant effect of genotype in 2-way ANOVA (p=0.0153). Boxes show median, quartiles and outlier fences for each dataset. Each data point represents one mouse. B) Paired t-tests were also used to compare cortical bone thickness between the loaded left limb and the non-loaded right limb for each Sptbn1 CKO and WT mouse. Uniaxial tibial loading induced a significant increase in Ct.Th, shown by a significant p-value for paired t-tests (p=0.0025), and when grouped by genotype, the Sptbn1 CKO mice showed a lower relative increase in Ct.Th as compared to the WT animals (p=0.0101). Each symbol shown represents the left (L) and right (R) tibia from one mouse. C) Representative microCT reconstructions for samples shown in Panel A.

Figure 8

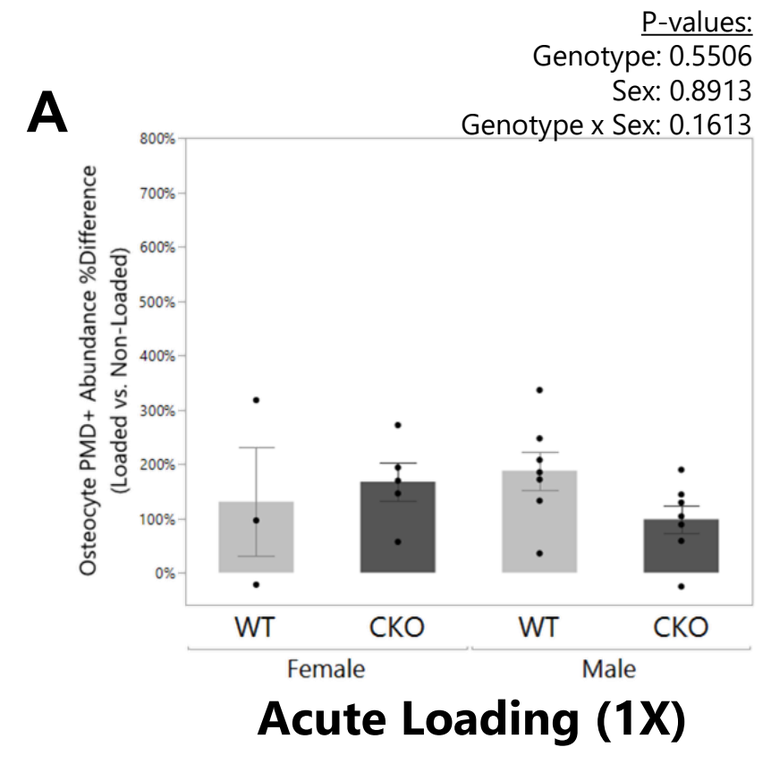

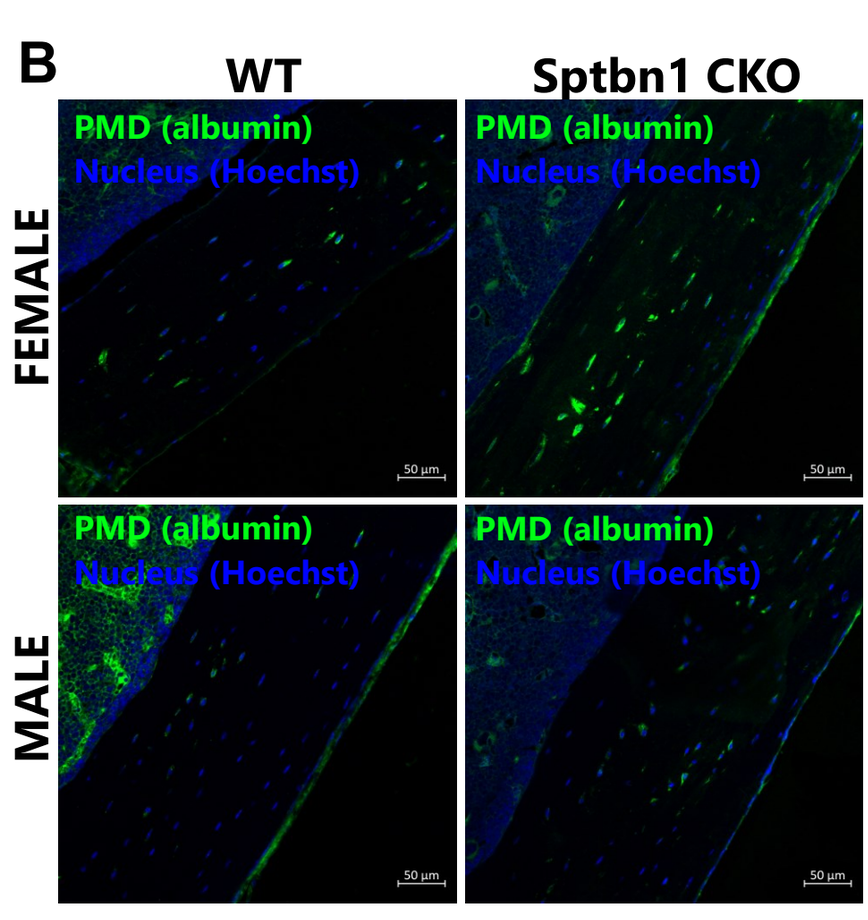

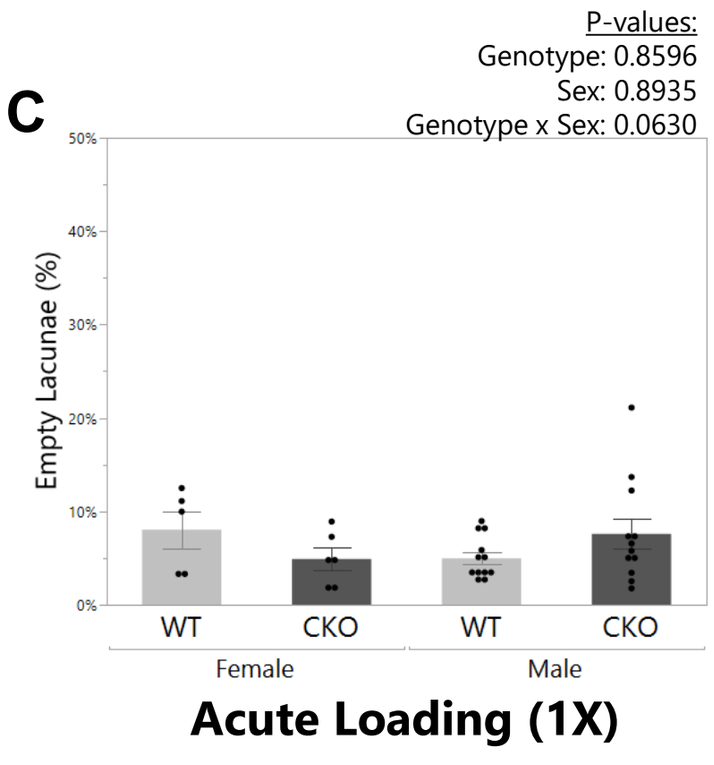

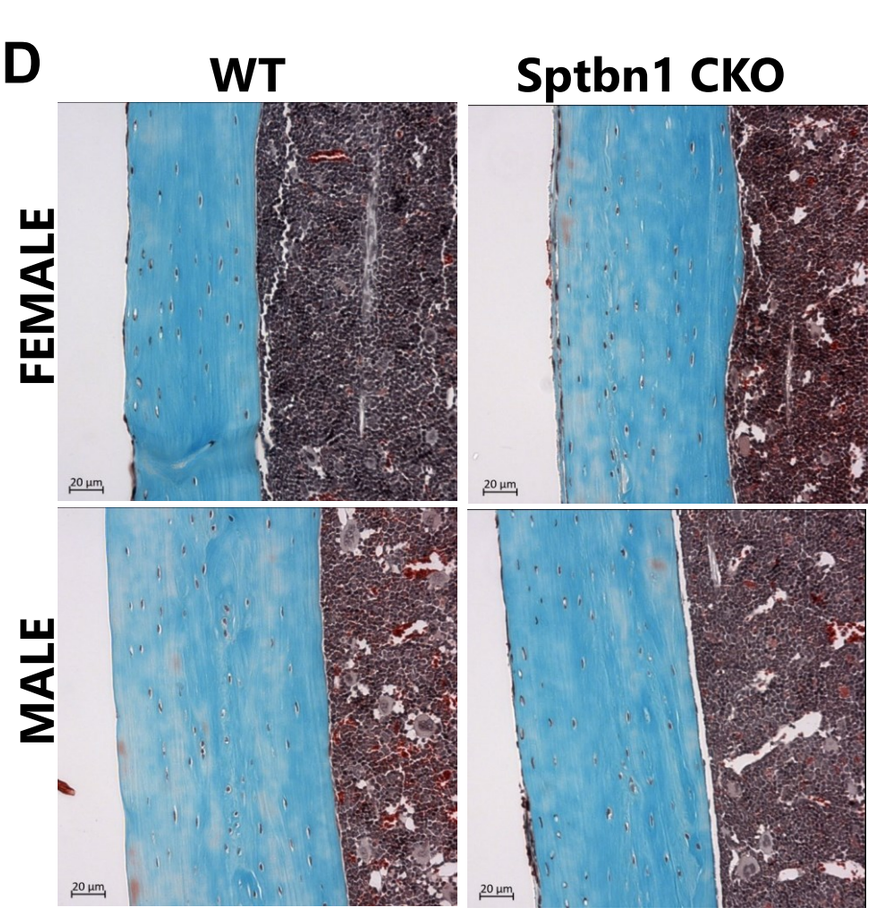

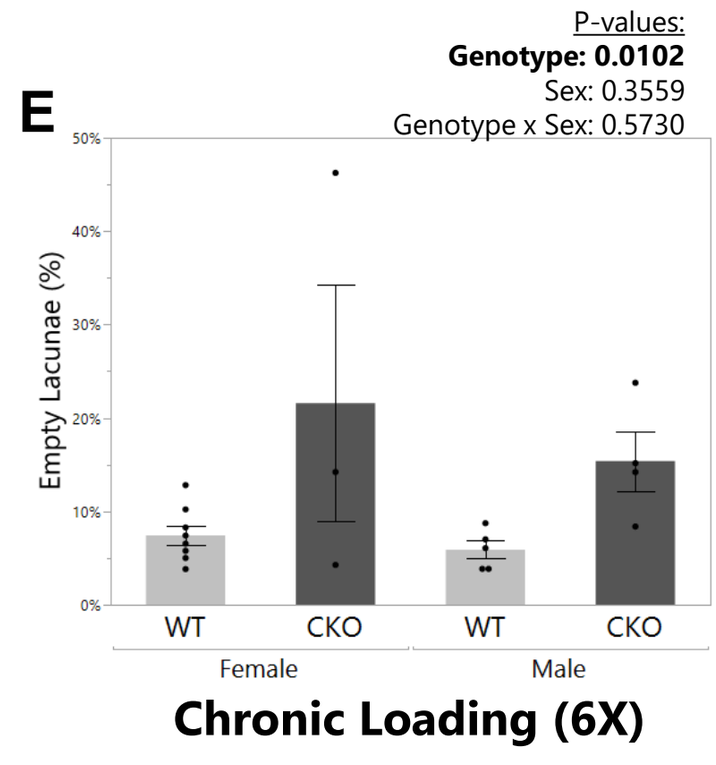

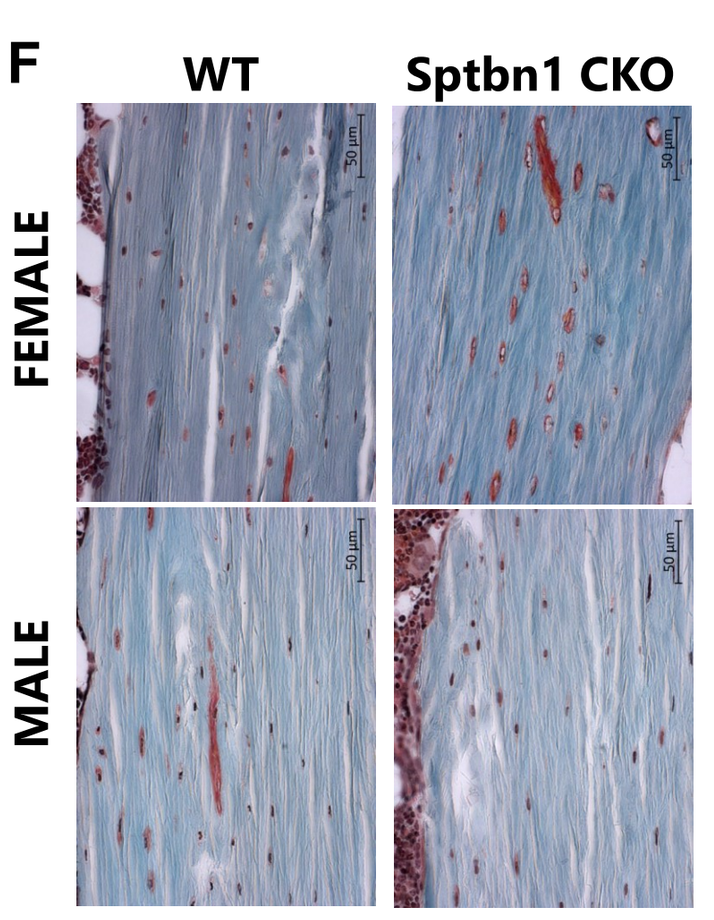

***Figure 8:** A) Although PMD were increased by loading (p paired t-test left vs. right <0.0001; not shown), the relative difference in PMD abundance between the loaded left limb and non-loaded right limb was not different between Sptbn1 CKO and WT mice (pgenotype = 0.5506). Bars show mean +/- SEM for each group; each dot represents one mouse. C) Representative images showing endogenous albumin quantified in panel A. C) Osteocyte lacunae vacancy in Sptbn1 CKO and WT mice subjected to uniaxial tibial loading. The relative number of empty osteocyte lacunae normalized to the total number of osteocyte lacunae was quantified in longitudinal sections loaded left tibias stained with Goldner's Trichrome. While no differences in the relative abundance of empty osteocyte lacunae were observed in mice subjected to one acute tibial loading bout (C-D; p=0.8596), both male and female Sptbn1 CKO mice showed more empty lacunae after 2 weeks of chronic loading (E-F; 6 loading bouts), as shown by a significant effect of genotype in 2-way ANOVA (p=0.0102).*

Supplemental Figure 1

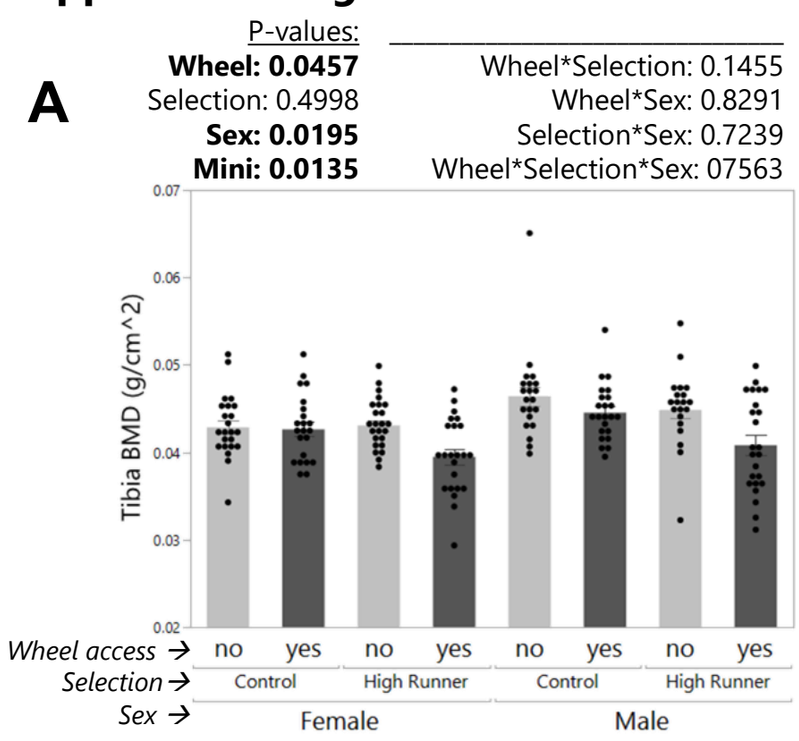

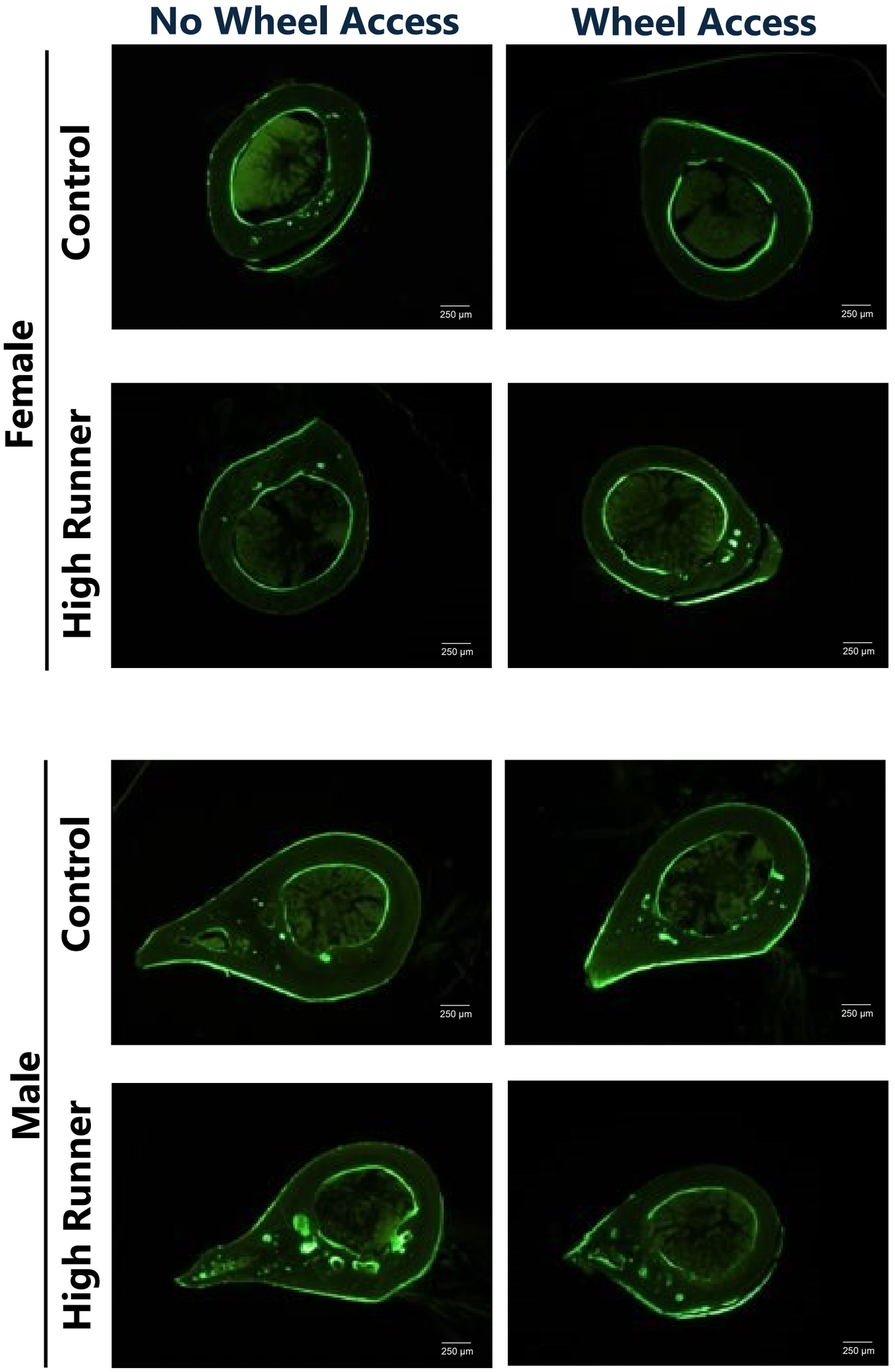

Supplemental Figure 1: *A) Bone mineral density in High Runner and control mice. Bone mineral density (BMD) was measured in the tibial mid-diaphysis by dual energy x-ray absorptiometry. Bars show mean +/- SEM for each group; each dot represents one mouse. Wheel access was associated with lower tibial BMD as shown by a significant effect of selection (p=0.0457). B) Representative images from the femoral mid-diaphysis showing cortical bone calcein labeling in High Runner and control mice.*

Supplemental Figure 2

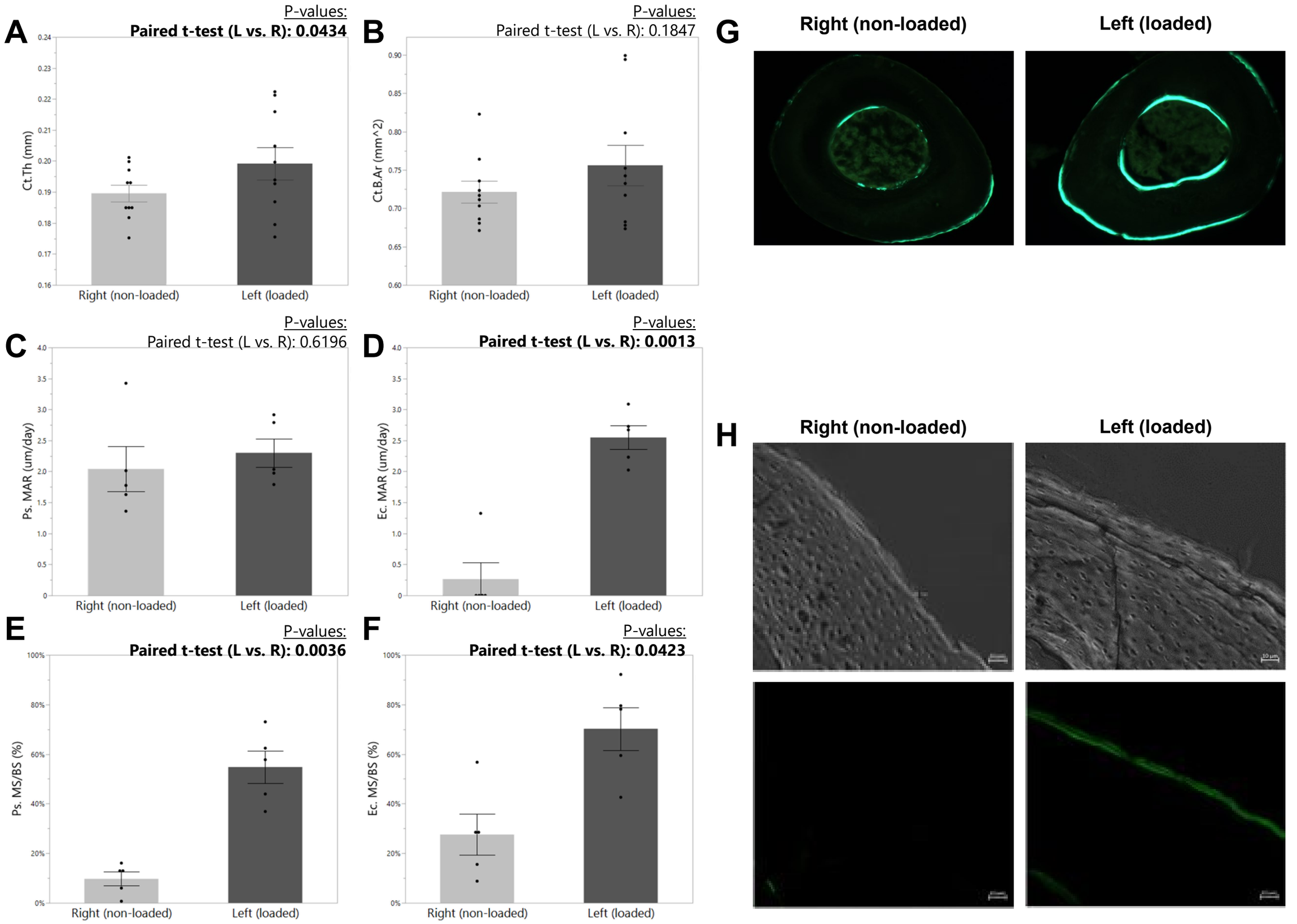

Supplemental Figure 2: Cortical bone geometry and dynamic histomorphometry in female CD-1 mice subjected to uniaxial tibial loading. *Female CD-1 mice were subjected to 2 weeks of uniaxial tibial loading beginning at 12 weeks of age. Bone properties in the left (loaded) versus right (non-loaded) tibia were compared for each mouse via paired t-tests. Micro-computed tomography was used to measure cortical bone thickness* ***(A)*** *and cortical bone area* ***(B)****. A subset of tibias was prepared for dynamic histomorphometric analysis of calcein labels, measuring periosteal and endocortical mineral apposition rates (****C-D****) and periosteal and endocortical mineralizing surfaces (****E-F****). Representative images are shown at low magnification in Panel* ***G*** *and at higher magnification in Panel* ***H****. Bars show mean +/- SEM for each group; each dot represents one mouse.*

Supplemental Figure 3

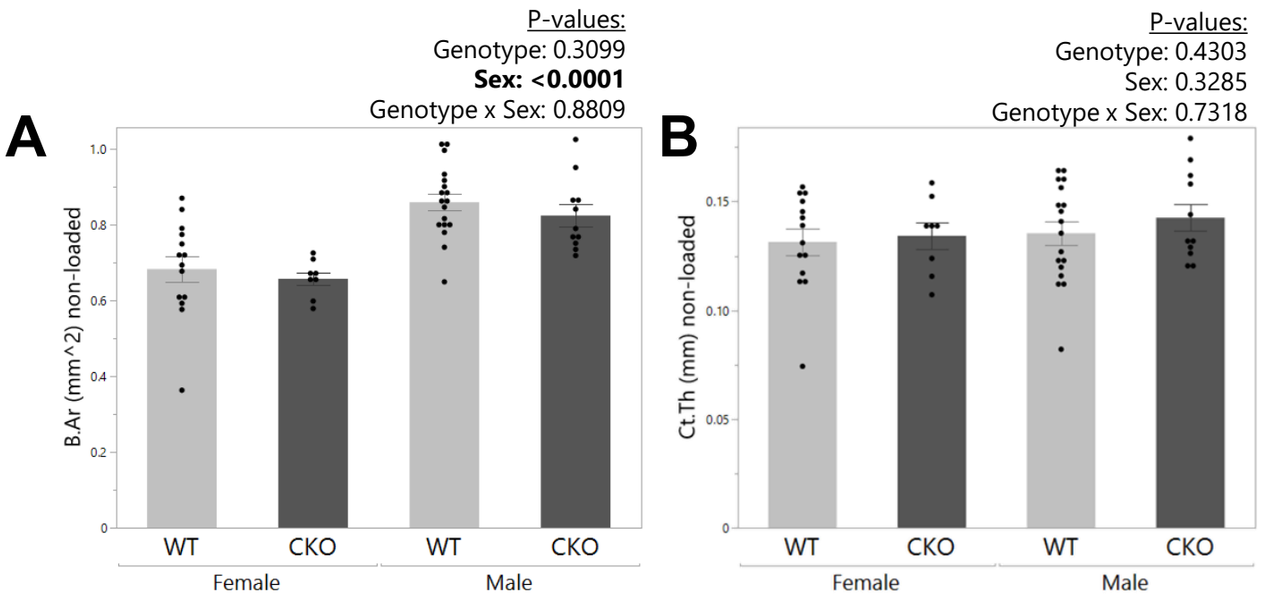

Supplemental Figure 3: Cortical bone geometry in the non-loaded right limb of Sptbn1 CKO and WT mice at 14 weeks of age. *Micro-computed tomography was used to measure cortical bone area* ***(A)*** *and cortical bone thickness* ***(B)*** *in the right (non-loaded) tibia of each mouse. Bars show mean +/- SEM for each group; each dot represents one mouse.*

SUPPLEMENTAL Figure 4

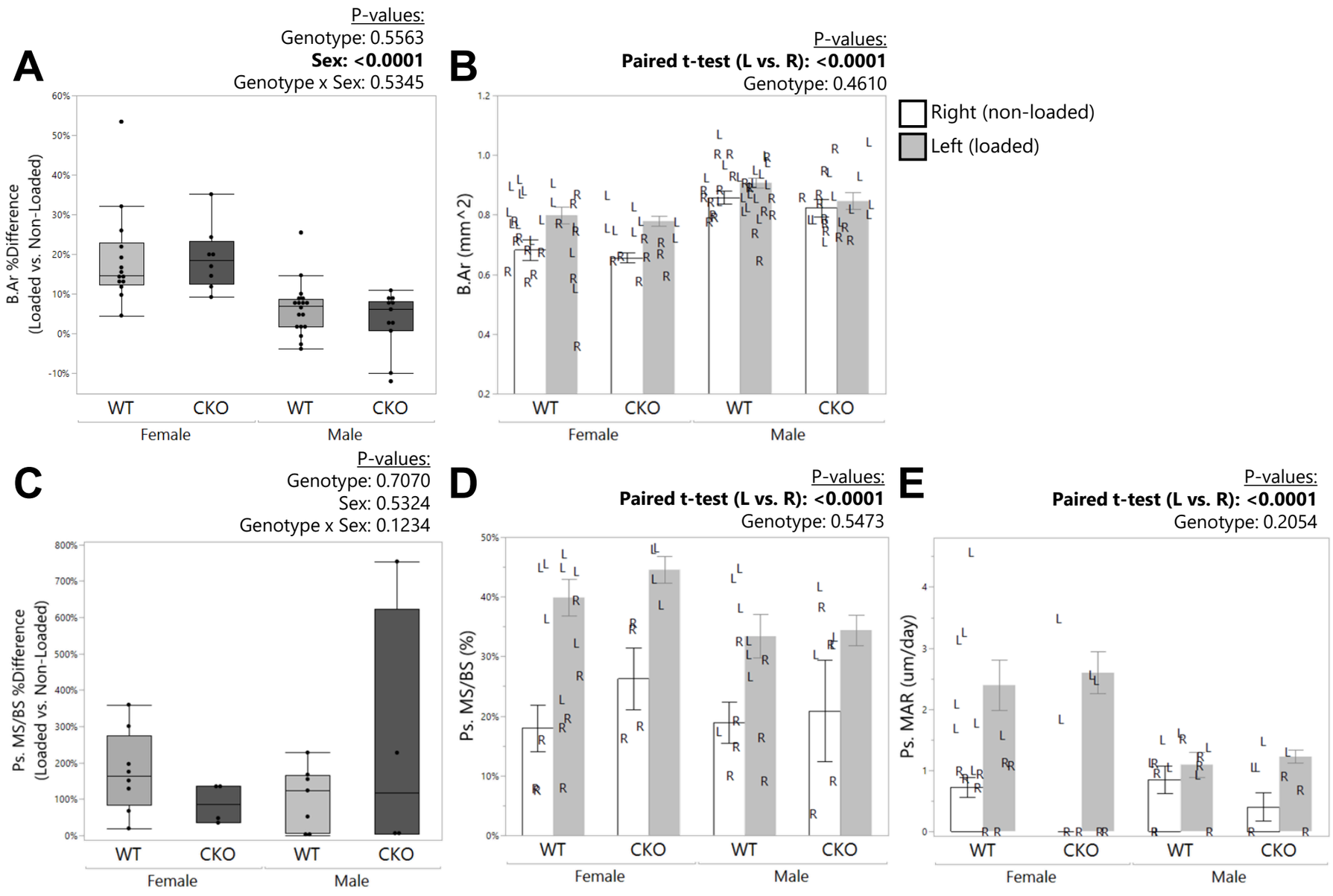

Supplemental Figure 4: Cortical bone geometry and dynamic histomorphometry in Sptbn1 CKO and WT mice subjected to uniaxial tibial loading. *Sptbn1 CKO and WT littermate mice were subjected to 2 weeks of uniaxial tibial loading beginning at 12 weeks of age. The percent difference in bone properties between the left (loaded) versus right (non-loaded) tibia was compared between male and female Sptbn1 CKO and WT mice with 2-way ANOVA, and the matched pairs comparison of bone properties between the left versus right tibia for each mouse was analyzed via paired t-tests with grouping by genotype for cortical bone area (**A-B**), periosteal mineralizing surface and mineral apposition rate (**C-E**), and endocortical mineralizing surface and mineral apposition rate (**F-H**). Percent difference was not calculated for mineral apposition rates due to an appreciable number of non-loaded right tibias lacking double labeled surface. Bars show mean +/- SEM for each group. Each dot (panels **A,C,F**) or letter (panels **B,D,E,G,H**) represents one mouse; L: left/loaded, R: right/non-loaded for pairwise comparison graphs.*